PLOS COMPUTATIONAL BIOLOGY

RESEARCH ARTICLE

Tumor vascular status controls oxygen delivery facilitated by infused polymerized hemoglobins with varying oxygen affinity

Donald A. Belcher[1], **Alfredo Lucas**[2], **Pedro Cabrales**[2], **Andre F. Palmer**[1]*

1 William G. Lowrie Department of Chemical and Biomolecular Engineering, The Ohio State University, Columbus, Ohio, United States of America, **2** Department of Bioengineering, University of California, San Diego, La Jolla, California, United States of America

* palmer.351@osu.edu

Citation: Belcher DA, Lucas A, Cabrales P, Palmer AF (2020) Tumor vascular status controls oxygen delivery facilitated by infused polymerized hemoglobins with varying oxygen affinity. PLoS Comput Biol 16(8): e1008157. https://doi.org/10.1371/journal.pcbi.1008157

Editor: Daniel A Beard, University of Michigan, UNITED STATES

Received: March 13, 2020

Accepted: July 16, 2020

Published: August 20, 2020

Data Availability Statement: All relevant data are within the manuscript and its Supporting Information files.

Funding: National Institute of Health grants R56HL123015, R01HL126945, and R01HL138116 were awarded to AFP and PC. National Institute of Health grant R01EB021926 was awarded to AFP. National Cancer Institute Grant R01CA188652 was awarded to PC; and the Pelotonia Graduate Research Fellowship was awarded to DAB. Any opinions, findings, and conclusions expressed in

Abstract

Oxygen (O_2) delivery facilitated by hemoglobin (Hb)-based O_2 carriers (HBOCs) is a promising strategy to increase the effectiveness of chemotherapeutics for treatment of solid tumors. However, the heterogeneous vascular structures present within tumors complicates evaluating the oxygenation potential of HBOCs within the tumor microenvironment. To account for spatial variations in the vasculature and tumor tissue that occur during tumor growth, we used a computational model to develop artificial tumor constructs. With these simulated tumors, we performed a polymerized human hemoglobin (hHb) (PolyhHb) enhanced oxygenation simulation accounting for differences in the physiologic characteristics of human and mouse blood. The results from this model were used to determine the potential effectiveness of different treatment options including a top load (low volume) and exchange (large volume) infusion of a tense quaternary state (T-State) PolyhHb, relaxed quaternary state (R-State) PolyhHb, and a non O_2 carrying control. Principal component analysis (PCA) revealed correlations between the different regimes of effectiveness within the different simulated dosage options. In general, we found that infusion of T-State PolyhHb is more likely to decrease tissue hypoxia and modulate the metabolic rate of O_2 consumption. Though the developed models are not a definitive descriptor of O_2 carrier interaction in tumor capillary networks, we accounted for factors such as non-uniform vascular density and permeability that limit the applicability of O_2 carriers during infusion. Finally, we have used these validated computational models to establish potential benchmarks to guide tumor treatment during translation of PolyhHb mediated therapies into clinical applications.

Author summary

High rates of oxygen consumption and abnormal vascularization lead to low oxygen levels within solid tumors. The lack of oxygen results in resistance to chemotherapies and increased rates of cancer progression. Hemoglobin-based oxygen carriers have the potential to increase the amount of oxygen delivered to tumors, which may make

this material are those of the author(s) and do not necessarily reflect those of the Pelotonia Fellowship Program. The funders had no role in study design, data collection and analysis, decision to publish, or preparation of the manuscript.

Competing interests: The authors have declared that no competing interests exist.

chemotherapies more effective. Unfortunately, translating experimental results from mice to humans is complicated by allometric scaling between mice and humans. To predict how these therapies may perform differently between human and murine systems, we computationally predicted how hemoglobin-based oxygen delivery varies between the two organisms. Our model accounts for how variations in the tumor vascular network impact the performance of hemoglobin-based oxygen carriers. This model also allows us to assess how the oxygen affinity of hemoglobin-based oxygen carriers affects the oxygenation of hypoxic tissue. The results of these models help us predict how results from murine models may translate to humans. Also, our models help to highlight what clinically-measurable tumor properties should be measured to predict the effectiveness of hemoglobin-based oxygen carriers in biological systems.

Introduction

The use of hemoglobin (Hb)-based oxygen (O_2) carriers (HBOCs) as a cancer chemosensitizing agent has been studied for a variety of prior generation HBOCs including crosslinked Hb (XLHb) [1–4],polymerized Hb (PolyHb) [5–12], surface conjugated Hb [13–16], and liposome encapsulated Hb [17–20]. In general, these studies have shown that HBOCs are effective at increasing O_2 delivery to tumor tissue. However, recent studies have demonstrated that HBOCs may not be efficacious for all tumor types or at specific dosage levels [21]. A time-line for the assessment of HBOC performance in oxygenating solid tissues is shown in Fig 1.

Despite three decades of work, no HBOC has translated into clinical treatment of tumor hypoxia. The stagnated development of HBOCs for use as a chemosensitizing agent is a result of both (1) inherent toxicity of previous generations of HBOCs and the (2) inconsistencies in hypoxia reduction in solid tumors. The toxicity of previous generations of HBOCs is associated with elevated renal toxicity and hypertension resulting from abundant stroma-free low molecular weight Hbs ($<$ 250 kDa) present within previous generations of HBOCs [22]. The presence of these low molecular weight species resulted in clinical failures during implementation of early generation HBOCs [23] Recently, HBOCs with higher molecular weights ($>$ 250 kDa) that are safer to infuse have been developed [12, 24, 25].

The ultimate goal of HBOC modulated oxygenation to tumors is to increase the effectiveness of O_2-dependent therapies such as chemotherapy. However, there are still concerns over inconsistent hypoxia reduction after HBOC infusion [21]. This inconsistency in O_2 transfer is likely a result of variations in vascularization and blood flow within tumors. Thus, quantifying how HBOC modulated oxygenation varies with clinically measurable properties of tumor vascularization may help guide development of clinical benchmarks of HBOC co-administration.

Unfortunately, determining these features with animal models alone necessitates the implementation of complex experimental methodology. For example, intravital microscopy techniques are able to examine transient changes within the tumor vascular structure. However, these models are typically geometrically limited to approximately two-dimensional tumor growth within chamber window models. Larger three-dimensional tumor growth relevant to human tissue is instead obtained by implanting tumors within host tissue and waiting for growth. Transiently measuring complete O_2 dynamics within the tumor structure might be performed with needle electrodes, positron emission tomography [26], and magnetic resonance imaging [27]. Another potential method to assess O_2 transport is optical mammography, an absorbance-based technique that determines the concentrations of Hb, oxygenated Hb (oxyHb), and deoxygenated Hb (deoxyHb) in breast tissue [28, 29]. Unfortunately, the spatial

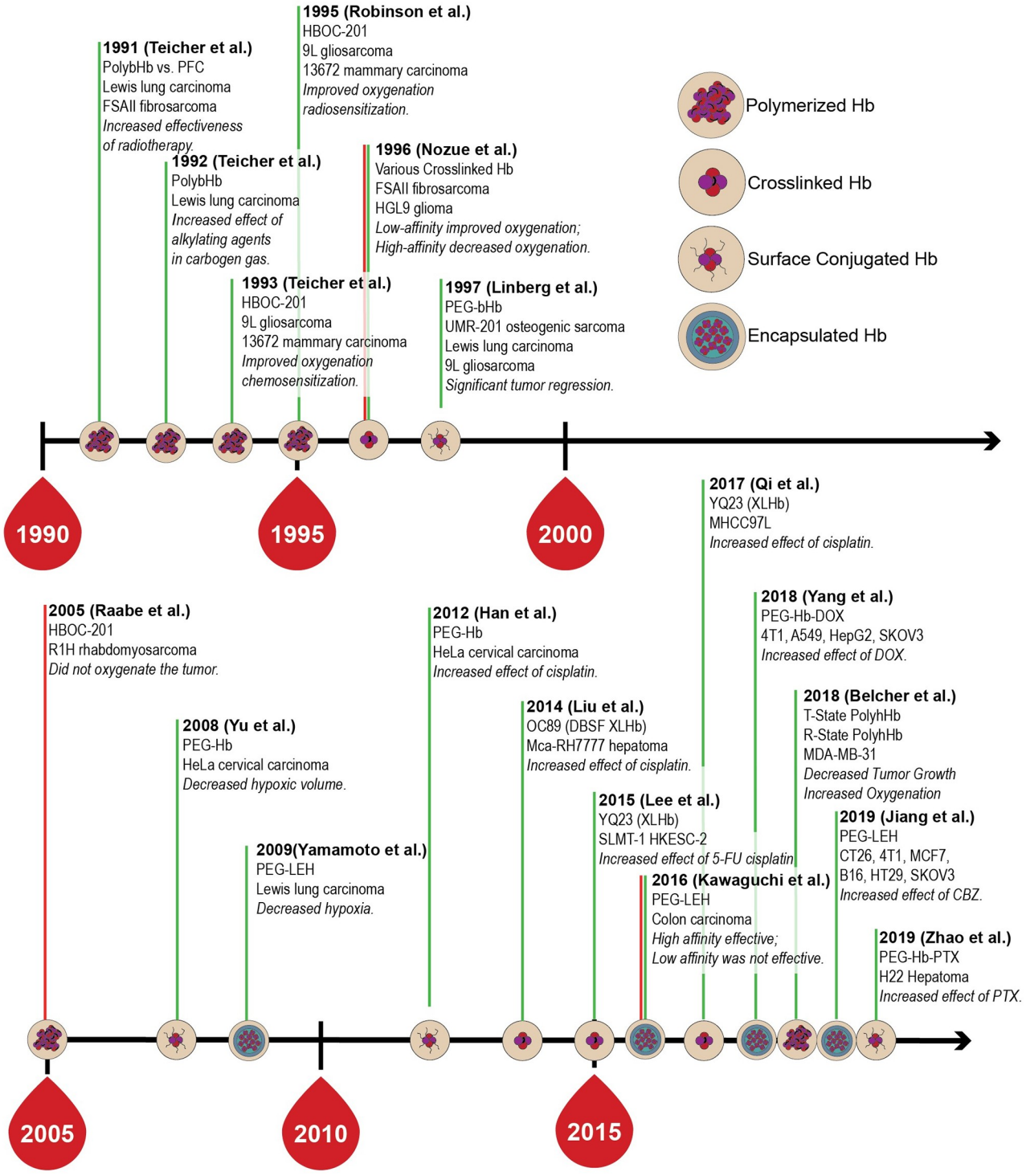

Fig 1. Time-line for the assessment of various HBOCs in the treatment of solid tumors. Green lines indicate positive results, red lines indicate negative results.

https://doi.org/10.1371/journal.pcbi.1008157.g001

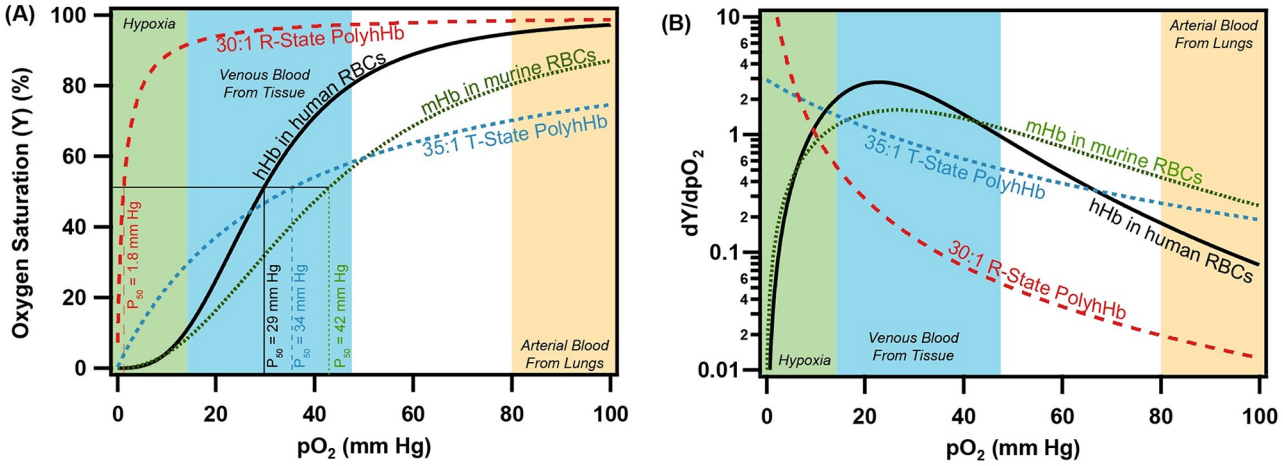

Fig 2. OEC and O_2 offloading plot for various O_2 carrying species used in the simulations. (A) The OEC is shown for human hemoglobin (hHb) in human RBCs, mouse hemoglobin (mHb) in mouse RBCs, 30:1 R-State PolyhHb, and 35:1 T-State PolyhHb. (B) The O_2 offloading plot as a function of the pO_2 is shown for the same species. Approximate pO_2 regions for arterial and venous blood under normoxic conditions have been included on this graph for reference.

https://doi.org/10.1371/journal.pcbi.1008157.g002

resolution of these methods are inadequate to resolve arterioles, venules, and capillaries. Instead these methods only allow us to estimate average O_2 and Hb concentrations within the bulk of tumor tissue.

Furthermore, commonly used small animal models, such as mice, have distinct physiologic differences in O_2 transport when compared to humans. These differences can be summarized by three alterations in fluid and mass transport when compared to humans: (1) decreased mouse red blood cell (RBC) size [30], (2) increased metabolic rate of O_2 consumption in the mouse host tissue [31–33], and (3) decreased O_2 affinity of mouse Hb in RBCs [34]. In mice, the decreased O_2 affinity of Hb in RBCs may result in reduced O_2 release from HBOC species in circulation when compared to HBOC performance in humans. An example of these changes in the O_2 equilibrium curvess (OECs) and the O_2 offloading plot as a function of partial pressure of dissolved O_2 (pO_2) is shown in Fig 2. The O_2 offloading plot demonstrates that both low O_2 affinity tense quaternary state (T-State) and high O_2 affinity relaxed quaternary state (R-State)polymerized human hemoglobin (hHb) (PolyhHb) may have lower rates of O_2 offloading compared to mouse RBCs under normoxic conditions. The O_2 offloading of both PolyhHb species only surpass O_2 offloading of mouse Hb in RBCs under hypoxic conditions (< 15 mm Hg). Though this increase in hypoxic O_2 offloading should be maintained under hypoxic conditions in humans, low O_2 affinity T-State PolyhHb should facilitate increased O_2 offloading in the arteries and arterioles of human subjects [12]. This fundamental difference in HBOC O_2 delivery potential may impact how results are translated from pre-clinical mouse models of HBOC infusion to clinical applications of HBOC infusion for cancer treatment. Thus understanding how the O_2 affinity of HBOCs influence O_2 transfer in humans is vital to understand how tumor oxygenation status may change if HBOCs are applied clinically.

From experimental studies of HBOC tumor treatment, we know that infusion of PolyHb results in a tumor growth delay [5–12]. This effect is thought to occur due to modulation of O_2 delivery at the host-tumor tissue interface. Unfortunately, there is an absence of clinically available data of these interfacial regions with adequate capillary resolution. Hence, computationally evaluating HBOC facilitated O_2 mass transport in a connected host tissue-tumor microenvironment is an exciting method to address how changes in the vasculature and host organism impact O_2 delivery modulation. However, any computational model we develop

must be able to translate the physical behavior of the O_2 carriers to host and tumor properties that are clinically measurable with current low-resolution imaging techniques. We hypothesize that parameters such as the concentration of oxyHb, regional blood volume (*RBV*), and regional blood flow (*RBF*) may predict how HBOCs modulate O_2 delivery to the tumor. Thus, this study aims to investigate how clinically measurable benchmarks might be useful to determine the oxygenation potential of T-State and R-State PolyhHb. To aid with predicting the effectiveness of PolyhHb within the heterogeneous tumor mass, we have redesigned an existing multi-scale 3D computational model of solid tumor growth and oxygenation to rapidly screen *in silico* the library of PolyhHbs in multiple simulated breast cancer tumors prior to *in vivo* analysis [35–39]. This newly developed model incorporates non-linear O_2 transport from both Hb in RBCs and HBOC in plasma. With this *in-silico* model, we explored how properties of the tumor micro-environment, including tumor growth, tumor density, and tumor location influence the oxygenation performance of various PolyhHbs. This is especially important because vascularization within solid tumors has a significant effect on O_2 and nutrient transport [40, 41]. Additionally, we can use these models to create physiological representations of both human and mouse tumors. We can then use these tumor models to assess how HBOC delivery in tumors may change when applied clinically.

Results

To test the oxygenation potential of PolyhHb within tumor microvascular networks, we implemented a modified version of the Tumorcode artificial tumor construct simulation framework [39] that incorporates O_2 transport from both Hb in RBCs and HBOCs. A flowchart of the simulation is shown in Fig 3.

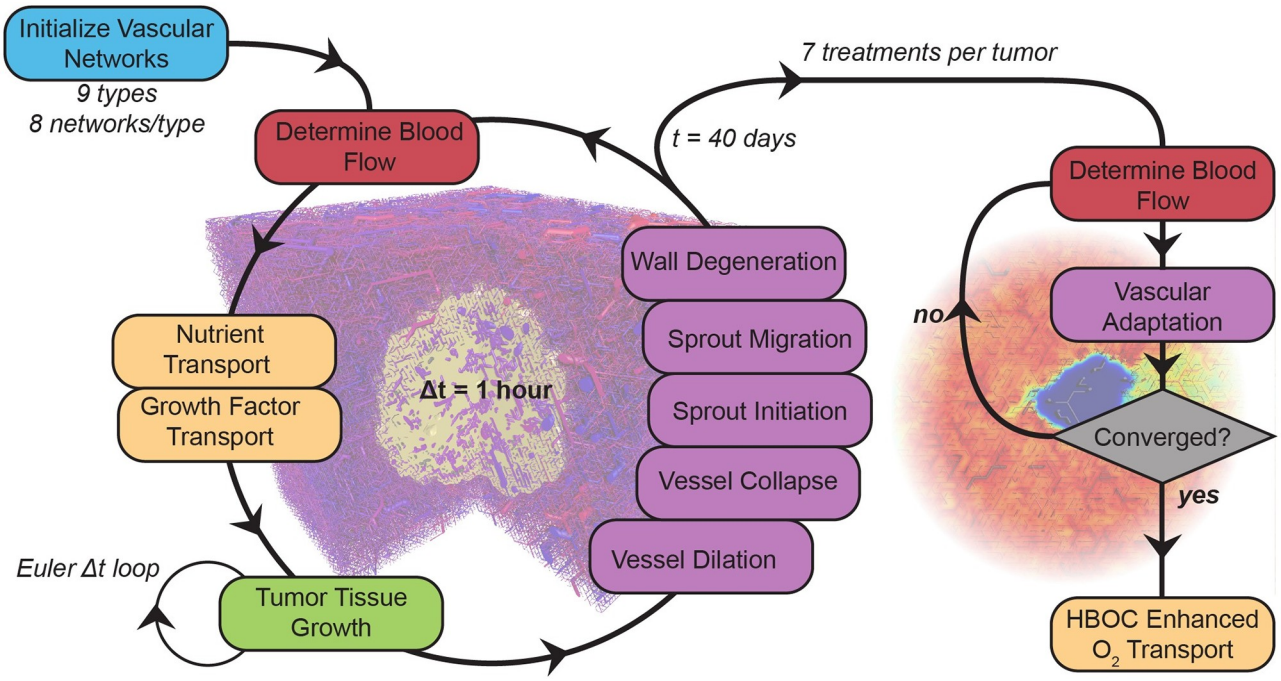

Fig 3. Model flow diagram. At each time step, blood flow, distribution of nutrients/growth factors and vascular remodeling are computed. The tissue phase remodels at shorter time steps within the main loop. The resulting artificial tumors are transferred to the infusion model. Hemodilution and the HBOC enhanced viscosity modulates flow and vascular adaptation until the microvascular system is stable. After this, HBOC enhanced oxygenation is modeled.

https://doi.org/10.1371/journal.pcbi.1008157.g003

Artificial tumor construct growth and properties

For these simulations, we began by generating artificial blood vessel networks with a variety of host tissues using constraint centered optimization on a face-centered cubic lattice. The method we use for generating the three-dimensional vascular structure follows methods previously described [39, 42, 43]. Variations in host structure approximate differences in experimental cohorts. Mouse and human 3D tumor constructs were generated using the continuum model for tumor growth and the simplified vascular adaptation model described in the S1 Appendix. Each tumor was generated within 6 mm wide cubic artificial vascular networks with 9 different artery/vein node configurations (Type A-I) (72 vascular beds). With the generated artificial vessel networks, we simulated 40 days of tumor growth with a multiphase continuum model for tumor expansion. This model of tumor tissue expansion consists of 5 phases: normal tissue, tumor tissue, necrotic tissue, extra-cellular matrix, and interstitial fluid. Both tumor growth and vascular remodeling were coordinated with a system of diffusible species representing nutrients and growth factors (i.e. O_2 and vascular endothelial growth factor (VEGF)) throughout the tissue space. During tumor growth, we model vascular deterioration and VEGF mediated angiogenesis modulated by changes in vascular fluid flow and VEGF stimulated vascular expansion throughout the vascular network.

Cross sections of depicting progression of the vascular network (blue), tumor tissue (green), and necrotic tissue (red) over a 40 day growth period for a tumor grown in a mouse type A vascular bed were used to examine the heterogenity of tumor growth. To quantify how artificial tumors progressed over 40 days of growth, various tumor properties including tumor radius, rate of radial expansion, tumor sphericity, necrotic volume%, *RBV* and Hb concentration in the tissue ($C_{Hb,tis}$) concentration in the tissue ($C_{Hb,tis}$) were recorded every 48 simulated hours during the growth of each artificial tumor construct. During tumor growth there was a correlative relationship in development of tumor *RBV* and tumor $C_{Hb,tis}$ during tumor expansion. The rate of radial expansion for Type D, E, and H tumors was higher than other vessel configurations. Visual examination of the combined tumor volume percentages (vascular:blue, tumor:green, necrotic:red) at the endpoint (t = 40 days)confirmed that the generated artificial tumors are topologically diverse with significant variations between vessel bed configurations. After visually confirming the heterogeneous composition of the artificial tumor constructs, the effect of tumor growth on remodeling of the vasculature was assessed with volume averaged properties. In general, tumor growth led to an increase in microvascular density (*MVD*), *RBV*, vascular surface density, and $C_{Hb,tis}$. A summary of these results is shown in Fig 4. Additional information on the cohort of artificially generated tumors can be found in the S2 Appendix.

Polymerized hemoglobin enhanced oxygenation

With the resulting artificially constructed tumor constructs, we simulated a PolyhHb mediated infusion with vascular adaptation and PolyhHb enhanced oxygenation. Here we simulated 7 infusion conditions for each artificially generated tumor construct. We simulated two dosing levels: a large volume exchange infusion and a low volume top-load infusion. To better examine performance of the materials, we analyzed a non-O_2 carrying control, a 35:1 T-State PolyhHb, and a 30:1 R-State PolyhHb. An unsupplemented baseline condition was also simulated to compare how the various infusions modulate O_2 delivery. To confirm if simulations were accurately modeling the O_2 distribution within the tumor we validated the simulation with intravital vascular pO_2 and Hb/PolyhHb saturation gathered from a mouse chamber window model as described in the S6 Appendix.

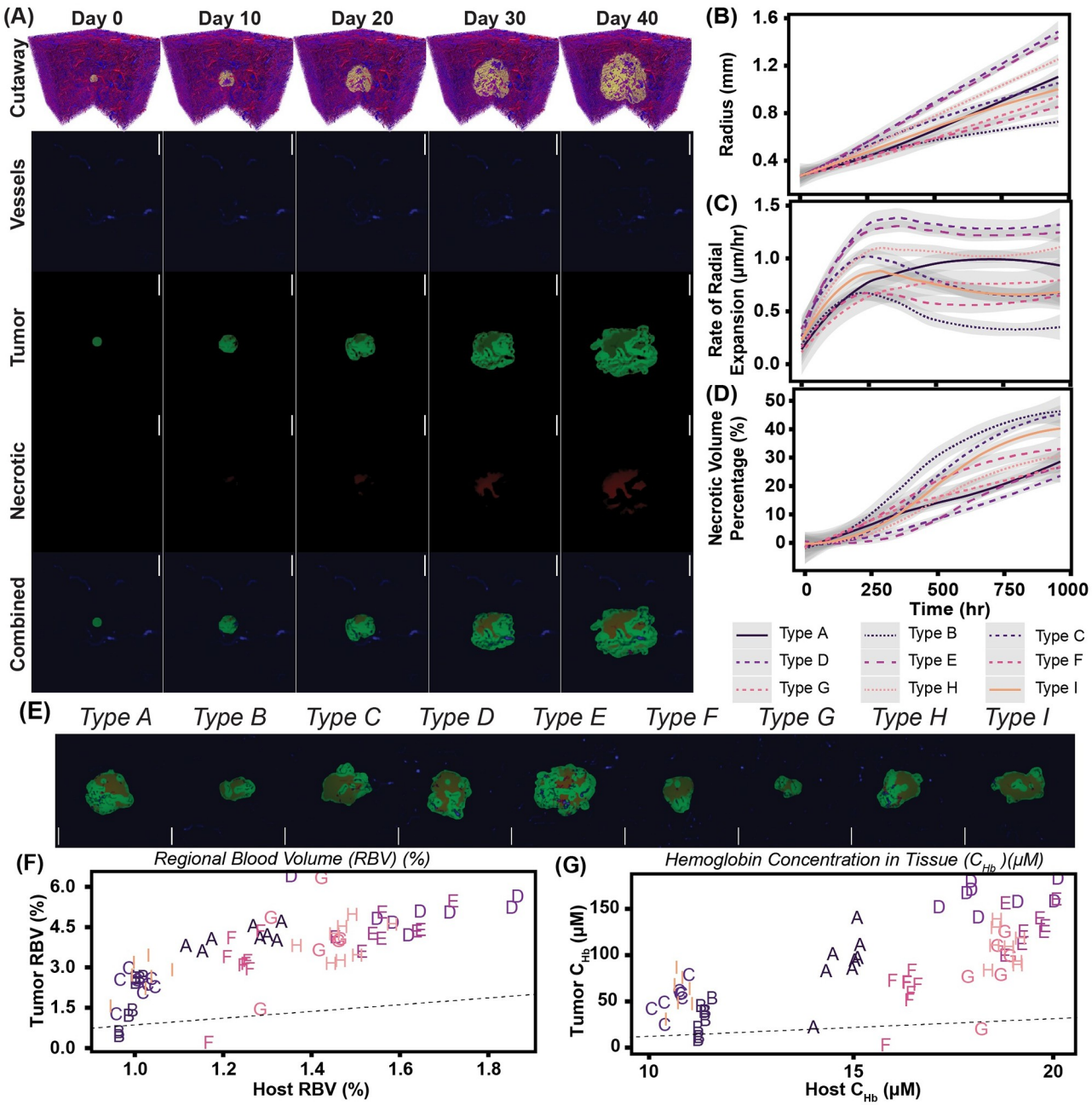

Fig 4. Artificial mouse tumor growth and resulting biophysical properties after 40 days of growth. (A) Visualization of cutaways, vessel (blue), tumor (green) and necrotic (red) volume fraction cross sections for artificial mouse tumor growth over 40 days. The tumor shown here was grown in a type A vascular bed. Also shown in this figure are the (B) radius, (C) rate of radial expansion, and (D) necrotic volume percentages for each vessel bed type (Type A-I). Shaded areas in these plots represent a 95% confidence interval across each type of vessel bed configuration. (E) Visualization of combined volume fraction cross sections for selected tumors from each of the vessel bed types (Type A-I). Comparison of (F) *RBV* and (G) $C_{Hb,tis}$ between the tumor and host tissue in the artificial tumor constructs. The letter labels indicate the vessel configuration. The dashed line separates the tumor properties greater than and less than the host properties. For all tumor cross sections the scale bar is 1 mm.

https://doi.org/10.1371/journal.pcbi.1008157.g004

Principal component analysis

To better predict correlation and grouping of spatially averaged and clinically measurable parameters in the simulation, principal component analysis (PCA) was performed on the

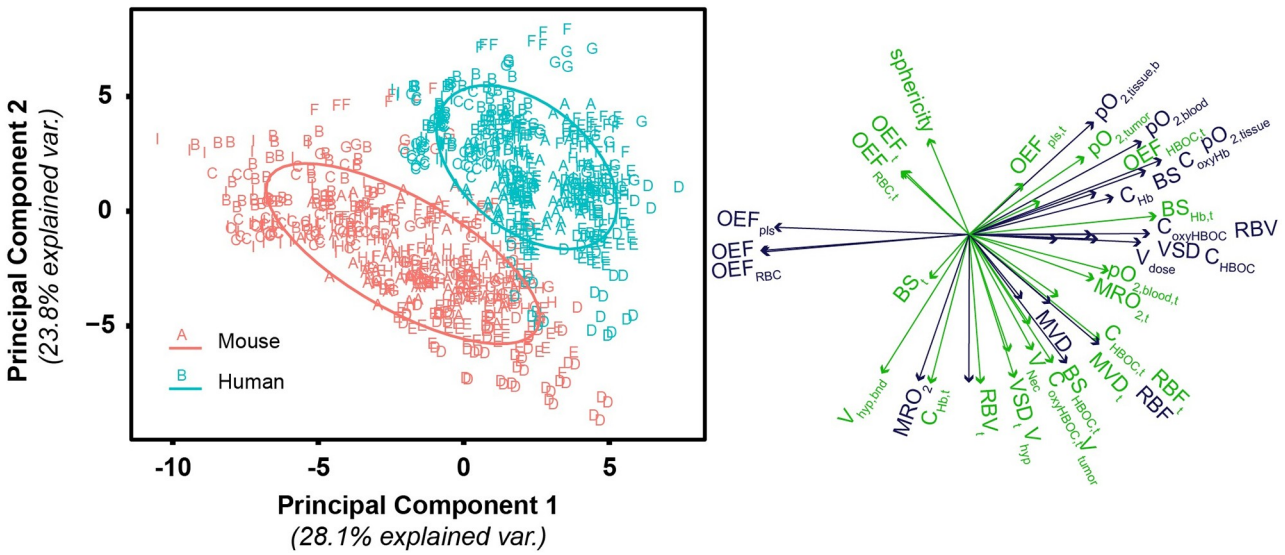

Fig 5. PCA biplot for principal components 1 and 2 of the mouse and human tumor model. In this figure, groupings are organized by organism type (human, mouse). Left: PC scores for tissue and O_2 delivery for each of the simulated tumor treatments. Ellipses are drawn around each group with 68% of the normal probability. Right: Loading plots relating how each parameter influences the corresponding principal component. Green vectors indicate tumor properties while blue vectors indicate host tissue properties. Labels indicate the corresponding tumor property.

https://doi.org/10.1371/journal.pcbi.1008157.g005

entire dataset of baseline and post-infusion tumors. Differences between mouse and human O_2 transport simulations are shown in Fig 5. The properties that separate the mouse and human tumor groups (tumor O_2 extraction fraction from HBOCs (OEF_{HBOC}, tumor tissue pO_2, and tumor blood saturation) are primarily linked to O_2 transport in the tumor. In comparison, properties that are relatively unchanged between the human and mouse group are overall O_2 extraction fraction (*OEF*), *MVD*, and *RBF*. There is significantly greater variance in artificially generated human tumors compared to artificially generated mouse tumors. Because of these differences, the data-set for the following analysis of tumor treatment are split between the two host organisms.

In mouse tumors, architectural and bulk properties of the tumor account for approximately 63% of the explained variance. Changes based on treatment type account for around 31% of the explained variance. A biplot for principal component 1 (PC1), principal component 2 (PC2), and principal component 3 (PC3) which shows these effects can be found in Fig 6. For PC1 and PC2,vascular bed type is used to group the tumors. In general, the different types of tumors are differentiated by *OEF*, O_2 extraction fraction from plasma (OEF_{plas}), O_2 extraction fraction from Hb in RBCs OEF_{Hb}, *RBV*, *RBF*, *MVD*, tumor volume, and necrotic volume percentage. In different vascular beds, there was differentiation based on O_2 properties, including hypoxic volume percentage and pO_2.

PC3 and PC2 account for approximately 31% of the variance in the simulated mouse tumors. Non-O_2 carrying control groups overlap with the baseline group. All PolyhHb infusion groups are separate from baseline and control groups. However, there is no significant difference between T-State and R-State PolyhHb at similar infusion dose volumes. Separation between these groups is dependent on OEF_{HBOC}, metabolic rate of O_2 consumption (MRO_2), and tumor tissue Hb saturation. Within these groups, the increasing dosages correlate with an increase in PolyhHb saturation and blood saturation. There is also a decrease in $C_{Hb,tis}$ with increasing dose volume.

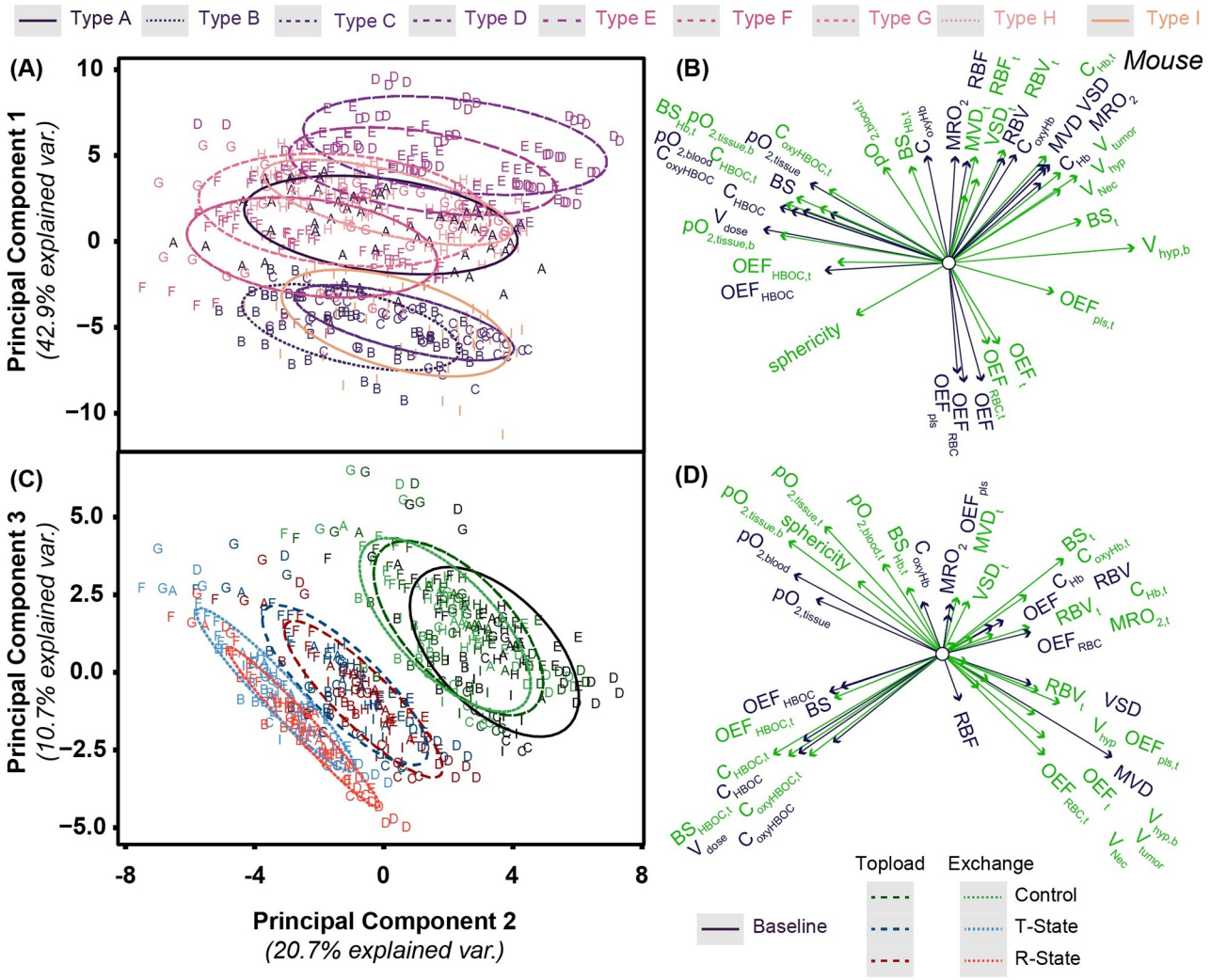

Fig 6. PCA biplot for principal components 1 and 2 for the analysis of the mouse model. PC scores for tissue properties and O_2 delivery for each of the simulated mouse tumor treatments for (A) principal component 1 and (C) principal component 3 as a function of principal component 2. Grouping in panel A is based on tumor vascular bed type. Grouping in panel B is based on dosing type. Ellipses are drawn around each group with 68% of the normal probability. Loading plots relating how each parameter influences the corresponding principal component is shown for (B) principal component 1 and (D) principal component 3 as a function of principal component 2. Loading vectors with magnitude less than 0.5 have been excluded from this plot. Green vectors indicate tumor properties while blue vectors indicate host tissue properties. Labels on each vector indicate the corresponding tumor property.

https://doi.org/10.1371/journal.pcbi.1008157.g006

In addition to PCA performed on mouse tumor data, PCA was performed on data from simulated human tumor constructs. A biplot of this analysis is shown in Fig 7. Compared to mouse data, there were similar trends observed in grouping and loading vectors of PC1 and PC2 depending on vascular bed configuration. For human tumors, there is significantly tighter grouping in loading vectors associated with vascular fluid flow and tissue oxygenation.

Comparison of simulated results

Changes in the vascular architecture of artificial tumors and resulting changes in Hb/PolyHb perfused tumor constructs after simulated infusions are shown in Fig 8. Both top-load and exchange infusion models result in significant ($p<0.05$) increases in *RBF*. Additionally,

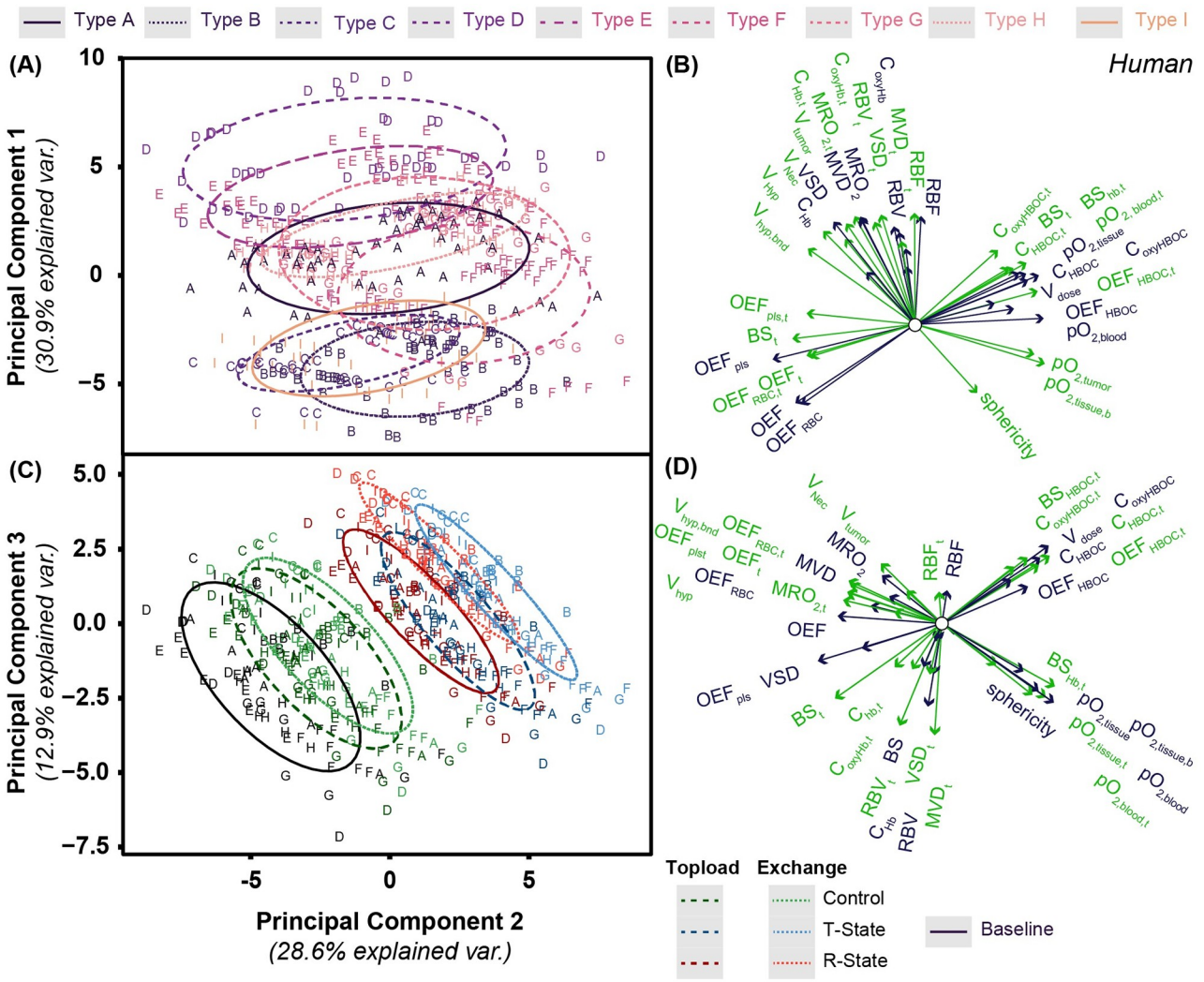

Fig 7. PCA biplot for principal components 1 and 2 for the analysis of the human model. PC scores for tissue properties and O_2 delivery for each of the simulated mouse tumor treatments for (A) principal component 1 and (C) principal component 3 as a function of principal component 2. Grouping in panel A is based on tumor vascular bed type. Grouping in panel B is based on dosing type. Ellipses are drawn around each group with 68% of the normal probability. Loading plots relating how each parameter influences the corresponding principal component is shown for (B) principal component 1 and (D) principal component 3 as a function of principal component 2. Loading vectors with magnitude less than 0.5 have been excluded from this plot. Green vectors indicate tumor properties while blue vectors indicate host tissue properties. Labels on each vector indicate the corresponding tumor property.

https://doi.org/10.1371/journal.pcbi.1008157.g007

exchange infusion significantly ($p<0.05$) increases *RBF* compared to top-load infusion. After top-load infusion, there is no significant change in *RBF* between different simulated treatment types. However, after exchange infusion, there is a significant difference between all simulated treatment types and the control. The 30:1 R-State PolyhHb treatment has the least improvement in *RBF* compared to other exchange infusion treatment options.

As expected from simulated hemodilution, all treatment types significantly ($p<0.05$) decreased $C_{Hb,tis}$. However, there are no significant differences between the control and PolyhHb treatments at the same dosage volume. Despite observing a decrease in $C_{Hb,tis}$, there is also a significant ($p<0.05$) increase in O_2 saturation of Hb in RBCs for all treatments compared to the baseline. During 35:1 T-State PolyhHb infusion, Hb saturation was significantly

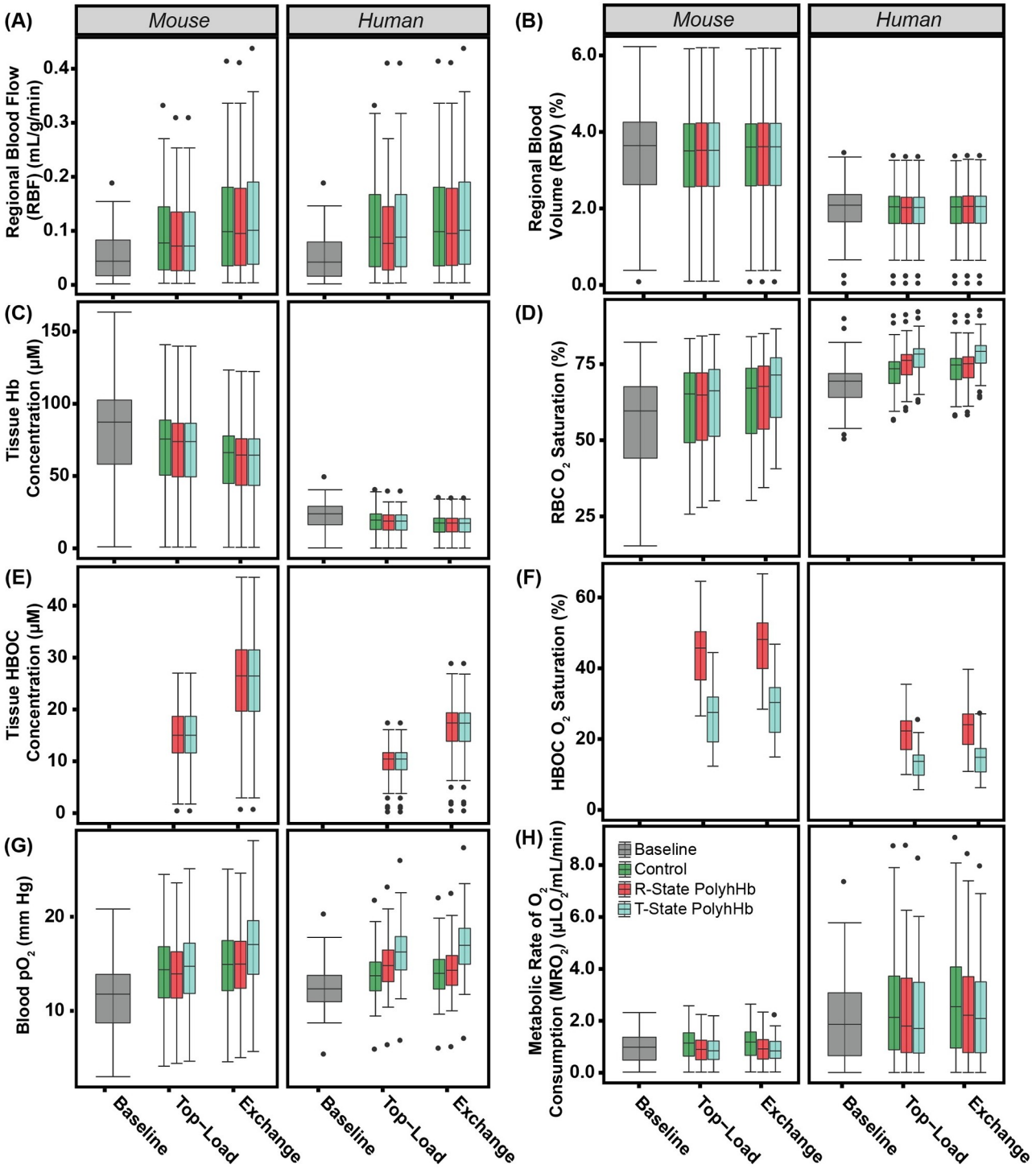

Fig 8. Changes in tumor vascular architecture and Hb/PolyhHb concentrations for the simulated PolyhHb enhanced infusion model. Variations in the (A) *RBV*, (B) *RBF*, (C) $C_{Hb,tis}$, (D) Hb O_2 saturation in RBC, (E) PolyhHb (HBOC) concentration, (F) PolyhHb (HBOC) O_2 saturation, (G) blood pO_2, and (H) MRO_2 for the baseline, top-load, and exchange infusion of the control, 30:1 R-State PolyhHb, and 35:1 T-State PolyhHb.

https://doi.org/10.1371/journal.pcbi.1008157.g008

($p<0.05$) greater than all other treatment options in both human and mouse models. Even though dose volume has a significant ($p<0.05$) effect on PolyhHb concentration in the tumor, there is negligible difference between the concentration of T-State and R-State PolyhHb at the same dose volume. As expected from the reduced *RBV* in the human model, the corresponding PolyhHb concentration is lower in human models compared to mouse models at corresponding dose volumes. Due to the low O_2 affinity of T-State PolyhHb, the concentration of O_2 saturated T-State PolyhHb is significantly($p<0.05$) less than the concentration of O_2 saturated R-State PolyhHb.

Additionally, vascular pO_2 within the artificial tumor significantly ($p<0.05$) increased in both top-load and exchange infusion models compared to the baseline. In mouse top-load dose simulations, there was no significant changes in vascular pO_2 between T-State PolyhHb, R-State PolyhHb, and the control. However, in the exchange infusion model, there is a significant ($p<0.05$) increase in T-State PolyhHb infusion compared to both R-State PolyhHb and control solutions.

The resulting changes in the *OEF*, OEF_{plas}, OEF_{Hb}, and OEF_{HBOC} are shown in Fig 9. Both top-load and exchange infusion models led to significant ($p<0.05$) decreases in *OEF* in both

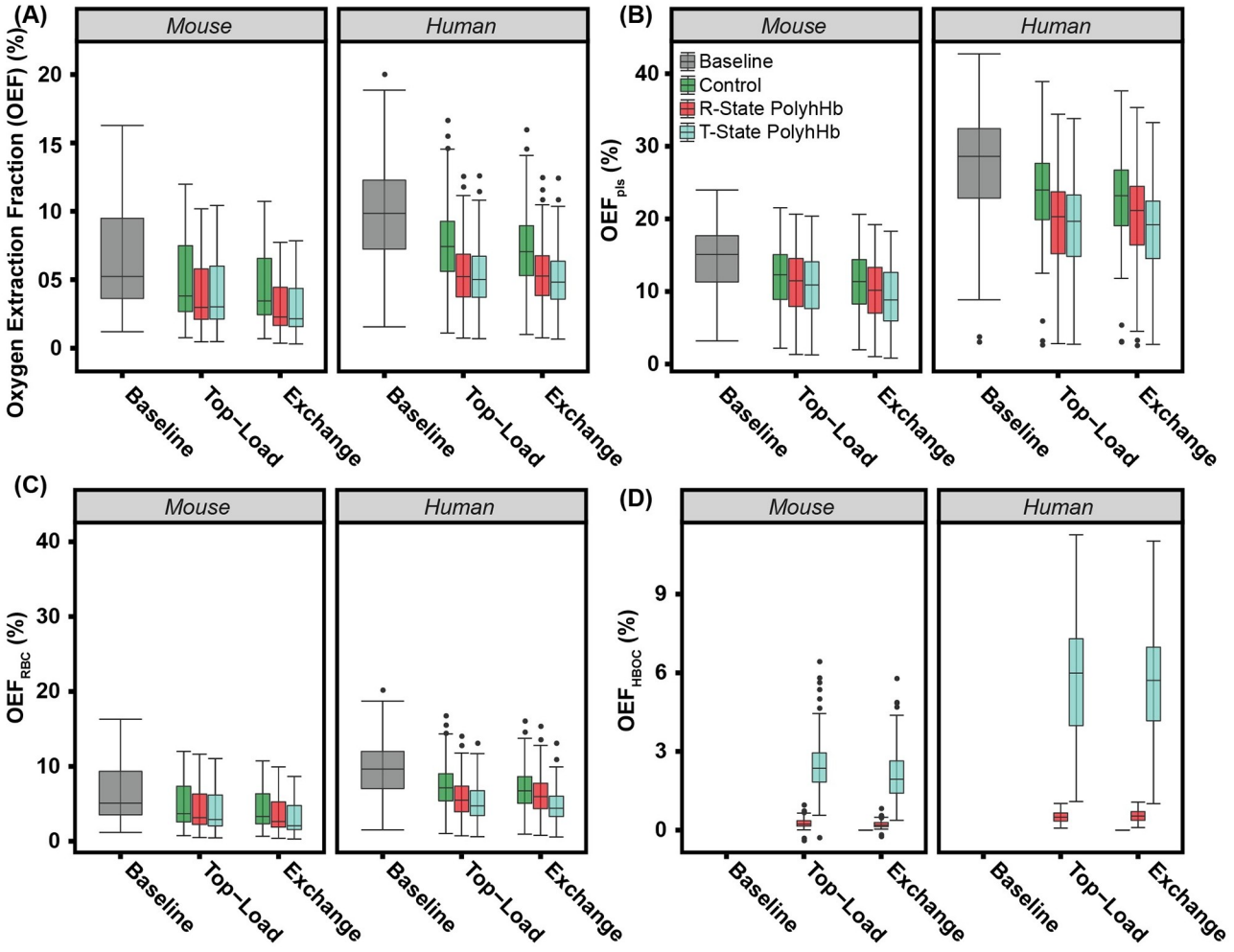

Fig 9. Changes in *OEF* for the simulated PolyhHb enhanced infusion model. Variations in (A) *OEF*, (B) Blood pO_2, (C) OEF_{plas}, (D) OEF_{Hb} O_2 saturation in RBC, and (E) OEF_{HBOC} (HBOC) concentration infusion of the control, 30:1 R-State PolyhHb, and 35:1 T-State PolyhHb.

https://doi.org/10.1371/journal.pcbi.1008157.g009

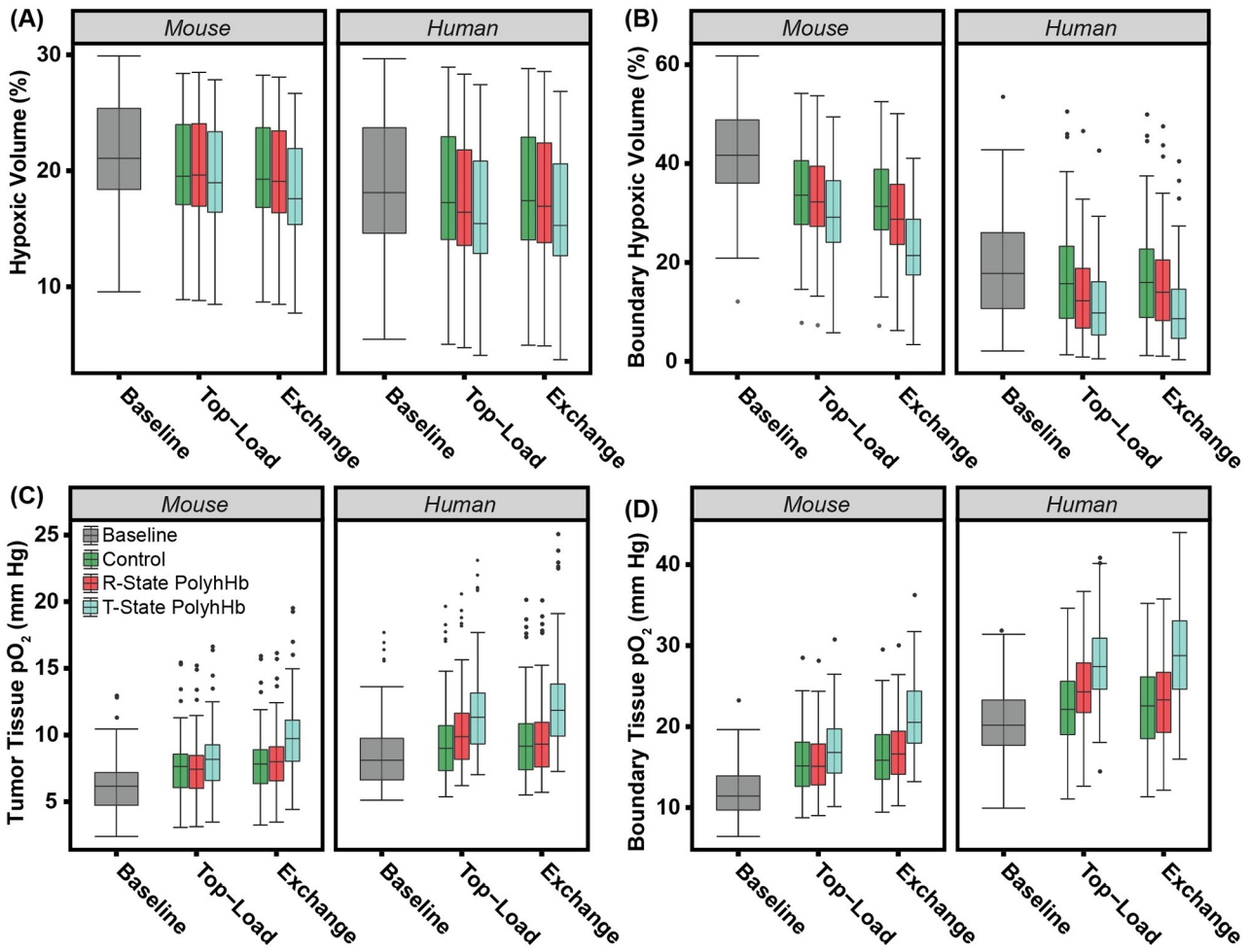

Fig 10. Changes in tumor hypoxia for the simulated PolyhHb enhanced infusion model. Variations in the (A) tumor tissue pO_2, (B) boundary tissue pO_2, (C) hypoxic fraction, and (D) boundary hypoxic fraction for infusion of the control, 30:1 R-State PolyhHb, and 35:1 T-State PolyhHb.

https://doi.org/10.1371/journal.pcbi.1008157.g010

mouse and human models. Despite the drastic difference in MRO_2, there is relatively little difference in *OEF* between mouse and human models. Infusion of 30:1 R-State PolyhHb and 35:1 T-State PolyhHb significantly ($p<0.05$) decreased *OEF* compared to the non O_2 carrying control infusions. There is no significant difference in total *OEF* between T-State and R-State PolyhHb. There are similar dose-dependent decreases in OEF_{plas} and OEF_{Hb}. However, T-State PolyhHb led to a significant ($p<0.05$) decrease in OEF_{plas} and the OEF_{Hb} compared to R-State PolyhHb. This decrease is offset by a significant ($p<0.05$) increase in T-State PolyhHb OEF_{HBOC} compared to R-State PolyhHb.

We calculated hypoxic volume fractions by taking the volume fraction of normal and tumor cells that are below a hypoxic threshold ($pO_2 < 5$ mm Hg). To match with literature approximations, we did not consider necrotic cells as part of the hypoxic volume. This is because necrotic cells are dead and thus do not have active hypoxia-inducible factors [44]. Changes in pO_2 and hypoxic volume fractions can be found in Fig 10. Tumor tissue pO_2 was significantly ($p<0.05$) higher in human tissue compared to mouse tissue. In both top-load and exchange infusions, there is a significant ($p<0.05$) increase in tumor tissue pO_2 and significant

($p<0.05$) decrease in hypoxic volume fraction for both control and PolyHb infusions. Infusion of 35:1 T-State PolyhHb resulted in a significant ($p<0.05$) increase in tumor tissue pO_2 compared to infusion of 30:1 R-State PolyhHb and control in both top-load and exchange infusion models. Despite observing this difference, there are no significant changes in hypoxic volume fraction between 35:1 T-State PolyhHb, 30:1 R-State PolyhHb, and control at both dose volumes.

In addition to the overall hypoxic fraction within the tumor for all of the treatment solutions, we also examined hypoxia within the tumor/host boundary region (volume fraction of tumor cells (ϕ_T) > 0 and volume fraction of necrotic cells (ϕ_D) = 0). In this region, both the top-load and exchange infusion models led to a significant ($p<0.05$) increase in tissue pO_2 and decrease in hypoxic volume fraction compared to baseline. In the exchange infusion model, 30:1 R-State PolyhHb infusion resulted in a significant ($p<0.05$) increase in tissue pO_2 and the hypoxic volume fraction compared to the control.

Performance thresholds

For this analysis, we compared the percent variation to the baseline conditions for each of the simulated infusion models. The percent change was calculated compared to the baseline ($\Delta\% = 100 \cdot (V - V_{BL})/V_{BL}$). For each of these systems, the properties of the baseline and post-infusion tumors led to a percent change in the hypoxic volume and MRO_2. For brevity, variables that did not significantly correlate with changes in the tumor oxygenation results were excluded from this analysis.

The effects of percent change in host tissue Hb saturation, percent change in tumor tissue Hb saturation, tumor *RBF*, and percent change in hypoxic volume are shown in Fig 11. The changes in boundary hypoxic fractions for 30:1 R-State PolyhHb infusion is clustered closer to the non O_2 carrying control than to 35:1 T-State PolyhHb for both mouse and human models. Top-load infusion of R-State PolyhHb result in equivalent hypoxic fraction reduction compared to the non-O_2 carrying control. In top-load infusion models we see relatively little correlation between *RBV* and the percent changes in the hypoxic volume when the *RBV* is above 0.1 mL/g/min. Decreases in the regional blood flow typically leads to greater reductions in the hypoxic fraction. Distinct groups were formed based upon Hb saturation decreases after infusion of R-State PolyhHb, T-State PolyhHb, or the non O_2 carrying control. Like the total tumor hypoxic volume, decreases in Hb O_2 saturation resulted in further decreases in the boundary hypoxic fraction for T-State PolyhHb and R-State PolyhHb. For mice, decreases in the percent change of the tissue Hb saturation led to increased boundary hypoxic reduction for T-State PolyhHb but not for R-State PolyhHb. In the human model, PolyhHb and both control solutions, the host tissue blood saturation had relatively little change on boundary hypoxic volumes. This indicates that even though changes in host tissue blood saturation may be predictive in small animal models. They will likely fail is used as performance thresholds when translated to clinical trials. Fortunately, the trends in boundary hypoxic reduction as a function of the percent change in tumor Hb saturation remains relatively unchanged. Additionally, there is a linear correlation between the percent decrease in the boundary and total hypoxic volume.

The effects of tumor oxyHb concentration, tissue blood saturation, *RBV* and *RBF* on changes in MRO_2 are shown in Fig 12. Unlike the hypoxic fraction, MRO_2 can either increase or decrease depending on dose volume, infused material, and tumor vessel bed configuration. In general, MRO_2 was increased in peripheral (type A, B, C, and I) vessel beds, whereas MRO_2 was decreased in distal and proximal (type D—H) vessel beds. This implies that tumor location relative to arteries and veins has a substantial effect on the resulting changes in MRO_2. Infusion

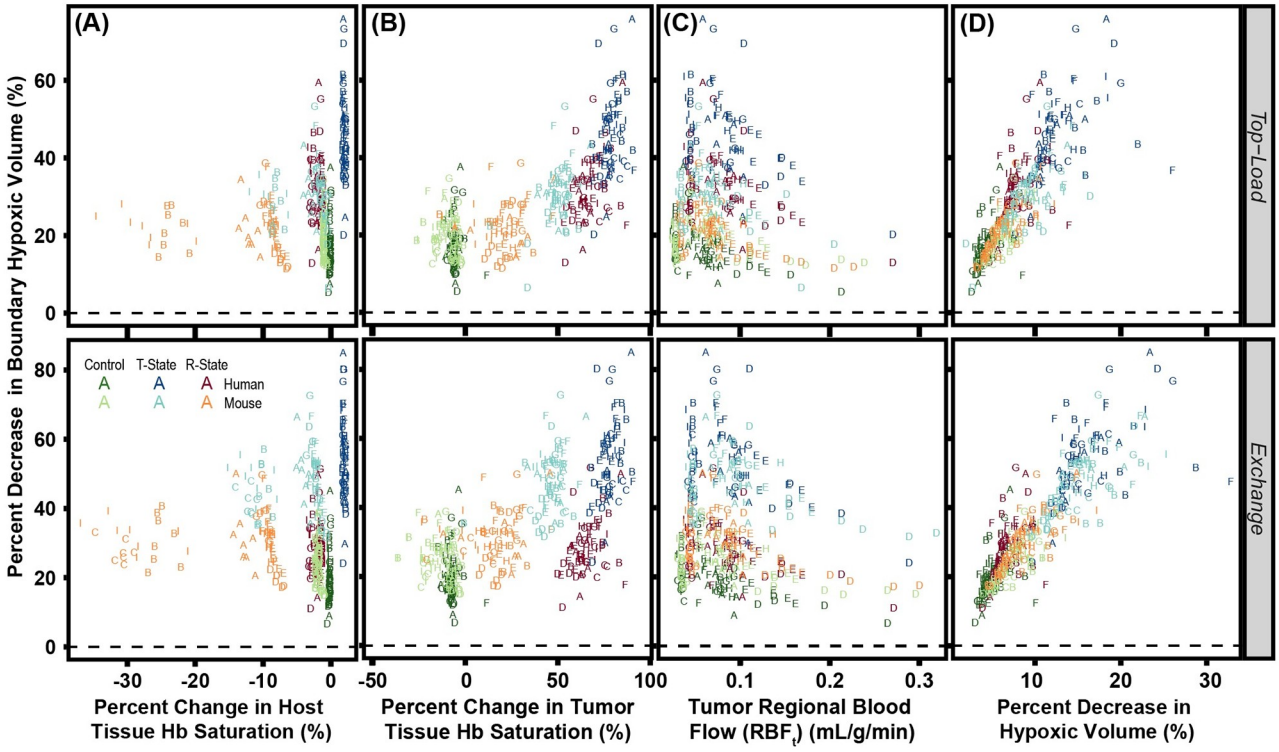

Fig 11. The effect of (A) host tissue Hb saturation, (B) tumor tissue Hb saturation, (C) tumor *RBF* and (D) percent decrease in total tumor hypoxic volume on the percent changes in the boundary hypoxic volume. The baseline (unsupplemented) condition is depicted as the dashed line at zero. Letters labeling each data point indicate the vessel bed configuration for that artificial tumor construct. The non O_2 carrying control is green, R-State PolyhHb is red, and T-State PolyhHb is blue.

https://doi.org/10.1371/journal.pcbi.1008157.g011

of non O_2 carrying controls always increases the MRO_2 in both mouse and human models. This effect is dose dependent with increased deviation from the baseline after exchange infusion. For both R-State and T-State PolyhHb, there are similar increases in the peripheral tumors. For these vascular beds, infusion of R-State PolyhHb does not lead to significant change in MRO_2. After infusion of T-State PolyhHb, MRO_2 dramatically decreased in the distal and proximal tumors.

In the human model, pre-infusion tissue oxyHb concentration and *RBV* are insufficient to significantly decrease the MRO_2. Similar to the effect of oxygenated Hb, we found that increasing pre-infusion O_2 saturation led to a decrease in MRO_2 change. Unlike *RBV* and oxyHb concentration, human and mouse data are not in agreement. At similar blood saturation values, the human model predicts an increase in MRO_2 whereas the mouse model predicts a decrease. For each treatment option increasing the *RBF* decreases the change in the MRO_2. For mouse tumors, we observed that *RBF* values greater than 0.1 mL/g/min may lead to reduction in MRO_2.

Discussion

The artificial tumors constructs generated in this study have significant variations in microvascular architecture. Despite observing a plateau in expansion rate, tumor growth is still approximately exponential. This is expected given that low tumor volumes (6.97 ± 5.11 mm^3) place them within the exponential region of tumor xenograft growth [45, 46]. The tumors need to be at least ten times larger before host tissue nutrient supply limits growth. Fortunately, the

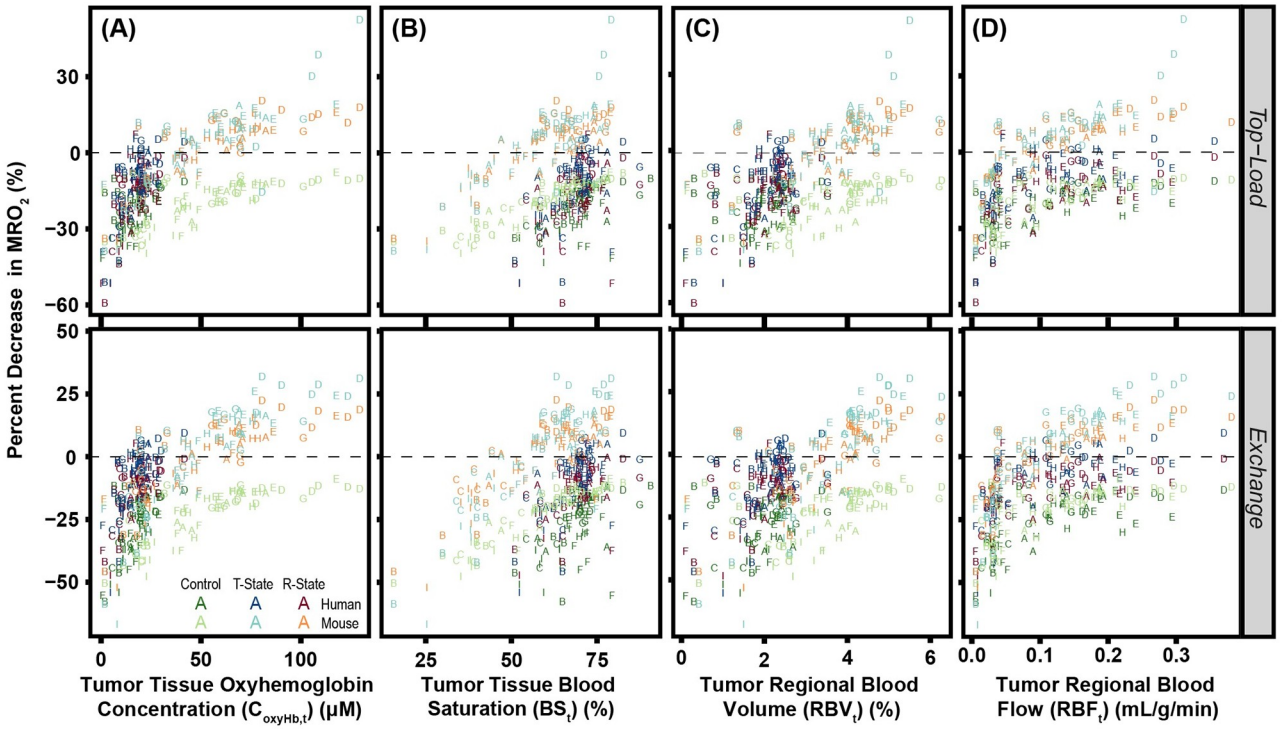

Fig 12. The effect tumor (A) oxyHb concentration, (B) tissue blood saturation, (C) *RBV*, and (D)*RBF* on the percent changes in MRO_2. The baseline (unsupplemented) condition is depicted as the dashed line at zero. Letters labeling each data point indicate the vessel bed configuration for that artificial tumor construct.

https://doi.org/10.1371/journal.pcbi.1008157.g012

tumor growth profile we observed matches data obtained with flat panel detector volume computed tomography (fpVCT) [47]. After simulating 40 days of tumor growth, most of the generated tumors have non-spheroid shapes with protrusions, oblong shapes, multiple clusters, and concave regions. As expected, tumor sections closer to arteries and large diameter arterioles tend to have less necrosis. Clusters of tumor growth have formed around these vessels as a result of increased regional O_2 supply. These structural changes are similar to variations in the bulk architectural properties of *in vivo* tumors.

Despite HBOC nitric oxide (NO) scavenging altering shear sensitivity in the vascular network, there is relatively little variations in *RBV* after simulated HBOC administration. This likely results from hemodilution decreasing blood viscosity and thus increasing *RBF*. The increased *RBF* increases the shear modulus and stabilizes the vascular network.

Oxygen transport

In mouse tumors we found that the angle between $C_{Hb,tis}$ and *RBV* loading vectors is relatively small, which indicates these factors are closely correlated. This is expected, given that increasing blood volume will also lead to an increase in the total volume of RBCs and thus the total mass of Hb found within the tumor. In contrast, the blood pO_2 vector is orthogonal to the necrotic percentage vector, which indicates that these variables are likely not correlated. Given that necrotic tissue does not consume O_2 (maximum rate of O_2 consumption ($V_M = 0$), we anticipated that increases in tumor necrotic fraction would have little effect on blood pO_2. The various bulk tumor properties including tumor volume, *RBV*, $C_{Hb,tis}$ and *RBF* are all tightly correlated. Additionally, tissue oxygenation variables are all partially correlated with both dose

volume and bulk tumor properties. This indicates that both tumor structural properties and dose volumes influence tumor oxygenation.

Compared to the control grouping in mouse tumors, the control group in human tumors was more similar to the PolyhHb treatment group. Additionally, in human tumors there was no clear separation between different volumes of PolyhHb infusion. Both R-State PolyhHb treatment groups are closer to the control when compared to the corresponding dose of T-State PolyhHb. This difference between the two PolyhHb species may indicate that T-State PolyhHb leads to more alterations in tissue oxygenation compared to R-State PolyhHb infusion. This effect is likely results from the O_2 affinity of T-State PolyhHb compared to the O_2 affinity of Hb in mouse and human RBCs. Because both T-State and R-State have lower O_2 affinity when compared to Hb in mouse RBCs they have similar performance. However, when compared to both R-State PolyhHb and the Hb in human RBCs, T-State PolyhHb has lower O_2 affinity. Additional evidence for these effects is demonstrated in alterations to O_2 saturation and *OEF* from Hb in RBCs and PolyhHb.

The values for RBC Hb O_2 saturation in the human model is comparable to experimental data measured by Grosenick *et al.* (74 ± 12%) [28]. The baseline RBC Hb O_2 saturation in the mouse model is significantly lower than the human RBC Hb O_2 saturation. However it is comparable to baseline RBC Hb O_2 saturation as measured in colon carcinomas in mice [18]. The change in Hb O_2 saturation after T-State and R-State infusion determined in these simulations is also in agreement with the the O_2 saturation of a low affinity (16 ± 10%) and high affinity (38 ± 8%) PEG-LEH as obtained with near infrared spectrocopy in a mouse colon carcinoma [18].

Similar to values of RBC Hb O_2 saturation, PolyhHb O_2 saturation is significantly lower in the human model when compared to the mouse model. This is likely a result of decreased *RBV* in the tumor coupled with an increase in RBC Hb O_2 affinity in the human tumor model. Despite having a similar average vascular pO_2 compared to the control, R-State PolyhHb appears to alleviate severe hypoxia is some tumors. After infusion of R-State PolyhHb in mouse tumors, the lowest average vascular pO_2 increased to 6.15 mm Hg from the baseline value of 2.4 mm Hg. This increase was more than what was observed after simulated infusion of a T-State PolyhHb (4.15 mm Hg). It is important to note that these conditions were observed primarily within the poorly vascularized type B, C, and I tumors, which may not be applicable to more mature tumors. In the human model, we instead observed that R-State PolyhHb increased blood pO_2 relative to the control similar to T-State PolyhHb in mice. In addition, T-State PolyhHb continued this trend with further increases in relative blood pO_2 compared to both the control and R-State PolyhHb in the human model.

Finally, the *OEF* vectors and *RBF* vectors are divergent, which indicates that these variables are negatively correlated. Increasing *RBF* decreases blood residence time within the tumor and increases O_2 mass transport through tumor tissue, which would lead to a decrease in O_2 extracted from blood. If we compare these loading vectors, increasing dose volume is positively correlated with increasing tumor and host tissue pO_2. The dose appears to be more closely correlated with boundary tumor tissue pO_2 than with host tissue pO_2. Although dose volume is also correlated with OEF_{HBOC} it is not correlated with the remaining *OEF*s. This is likely because tissue O_2 demand is relatively unchanged even after increasing simulated dose volume. In the human model, T-State PolyhHb had much greater O_2 extraction. In comparison, R-State PolyhHb had relatively similar O_2 extraction in the mouse and human models. Additionally, the dose volume has negligible effect on OEF_{HBOC}.

Despite delivering a greater fraction of its O_2, T-State PolyhHb still delivers significantly less of its O_2 compared to Hb in RBCs. This is expected because the partial pressure of O_2 at

which 50% of the hHb or PolyhHb is saturated with O_2 (P_{50}) of 35:1 T-State PolyhHb (34 mm Hg) is still less than P_{50} of mouse Hb in RBCs (42 mm Hg). Because of this increased P_{50}, mouse Hb will, on average, deliver more O_2 than T-State PolyhHb under elevated O_2 tensions. Thus we expect that OEF_{HBOC} would increase for both of the species as the OEF_{Hb} approaches complete O_2 delivery ($OEF_{Hb} \rightarrow 100\%$) under highly hypoxic conditions ($pO_2 \rightarrow 0$ mm Hg). Because of this increase in OEF_{HBOC} in the human models, we anticipate that T-State PolyhHb may be more effective at oxygenating tumors in humans.

Tumor hypoxia

The lack of a dramatic decrease in overall tumor hypoxia is not in agreement with data from Teicher and Robinson *et al.* [5, 8, 9]. In these studies, the hypoxic fractions (< 5 mm Hg) under baseline conditions in the 13672 mammary carcinomas was 53% of tumor readings, and the 97 gliosarcomas was 49% of tumor readings. After infusion of low-affinity polymerized bovine Hb (bHb) (PolybHb) HBOC-201, these studies found the hypoxic readings decreased to 40% of total readings for the 13672 mammary carcinomas and 24% for the 9L gliosarcomas. However, the needle O_2 electrode used in these studies had a maximum depth of 1 mm, which is still in the tumor periphery of 100 mm^3 tumors.

In the boundary region between tumor and host tissue, we observed an increase in tissue pO_2. However, there is considerably more hypoxic volume within this region. This primarily results from no longer including regions that are necrotic in our hypoxia evaluation within this region. These necrotic regions comprise a significant percentage (20 to 50%) of the simulated tumor mass. In both top-load and exchange infusion models, the presence of 35:1 T-State PolyhHb led to significant increases in boundary tissue pO_2 and decreases in boundary tissue hypoxic volume fraction. This indicates that T-State PolyhHb is likely much more effective at oxygenating these tumors than either the non O_2 carrying control or R-State PolyhHb.

Within this region, our results from the mouse model match trends observed by Teicher and Robinson *et al.* [5, 8, 9]. We also observed similar trends in the oxygenation for our model at the baseline pO_2 (average of 12.5 mm Hg) and the exchange T-State PolyhHb infusion (18 mm Hg) compared to the early experimental data at the baseline (11.3 mm Hg) and the low-affinity HBOC infusion (20.8 mm Hg) [8]. This increase in the boundary region oxygenation may be related to the tumor growth delay observed after HBOC infusion in many of the previous experimental studies. Increased oxygenation of the tumor periphery can lead to increased survival of the host cells [48], which may result in the experimentally observed tumor growth delay.

Aditionally, the percent change in the total Hb saturation may be a predictor of increased hypoxia reduction for R-State PolyhHb. Decreases in the Hb saturation after T-State PolyhHb infusion translated to significant reduction in hypoxic volume. Unfortunately, this trend does not translate to R-State PolyhHb. For R-State PolyhHb there was no significant change as the tissue Hb saturation decreased. This is likely because the high O_2 affinity R-State PolyhHb has relatively minor O_2 release compared to T-State PolyhHb. Because of this, total Hb saturation is likely a poor marker to evaluate potential effectiveness of any high affinity O_2 carrier for tumor oxygenation.

We also found the low *RBF* led to increased boundary hypoxia reduction. Typically, increases in the *RBF* is thought to increase tumor exposure to the circulated drug and thus its overall effectiveness [49]. This increase in efficacy is thought to occur due to an increase in O_2, nutrient, and drug transport into tumor tissue. However, the reason we observed the performance enhancements associated with treatment models in this study is likely related to

inadequate initial oxygenation of tumor tissue. For example, tumors with low initial *RBF* will likely be poorly oxygenated due to decreased exposure to circulating Hb in RBCs. Infusing a significant volume of PolyhHb increases the *RBF* via hemodilution, which will lead to greater decreases in the hypoxic volume of these tissues. Pre-infusion *RBF*s less than approximately 0.050 ml/(g min) in the top-load infusion model and 0.075 ml/g/min in the exchange infusion model were required but does not imply an increased reduction in the hypoxic volume.

Metabolic rate of oxygen consumption

The tumor MRO_2 was approximately two times higher in the human model when compared to the mouse model. This is in agreement with the increase in O_2 consumption in humans under hypoxia [31, 50, 51]. This is likely a result of significantly decreased O_2 release from the mouse Hb in RBCs under hypoxic conditions when compared to trends in the literature [31]. Additionally, the mouse host tissue MRO_2 was significantly greater than human host tissue MRO_2 (Data shown in S4 Appendix). Simulated infusion of the non-O_2 carrying control lead to increases in the MRO_2. The MRO_2 was relatively similar between baseline and after T-State PolyhHb infusions.

Based on analysis of changes in tumor MRO_2, we can predict that the proximal and distal tumors are typically more susceptible to MRO_2 reduction compared to tumors growing in the periphery of arterial venous connections. This variance in MRO_2 may contribute to the tumor growth delay observed in various animal studies [6, 8, 9]. Attenuating O_2 consumption in tissue can also lead to decreases in the cell proliferation rate [52]. The oxyHb concentration would need to be above at least 45 μM before decreased MRO_2 would be observed. Additionally, tumor *RBV* would likely need to be above 2.5 percent before these effects are observed in humans. In distal and proximal tumors (Types D-H), there is a dramatic divergence in the different treatment types depending on the oxyHb concentration. We also examined how pre-infusion Hb O_2 saturation can predict changes in MRO_2. The discontinuity between changes in mouse and human MRO_2 indicates that comparing the tissue blood saturation between mice and humans may not fully represent the O_2 status of the tissue. A similar trend is observed for the effect of tumor *RBF* on MRO_2. For PolyhHb perfused human tumors and all control groups, we never observe a decrease in MRO_2 compared to baseline conditions. This difference between tumors in different species is likely the result of the decreased Hb O_2 affinity in murine RBCs which results in decreased *OEF* and $C_{Hb,tis}$ despite increased *RBF* and O_2 saturation. Thus, we predict that changes in MRO_2 consumption should not be predicted via analysis of blood O_2 saturation or *RBF*.

Comparison with previous computational models

Previous computational models of vascular O_2 transport to tumors extend upon previously developed Krogh tissue cylinder (KTC) models by instead modeling O_2 and blood transport throughout an entire arterio-venous network connected by a capillary bed [53]. Early versions of these models used a Green's function method to model O_2 transport throughout a capillary network [54–56]. In general, these morphologically complex models gave more physiologically accurate estimations of hypoxia compared to the KTC models. [56]. This type of O_2 transport model was used to explore the effects of changing the Hb O_2 affinity on tissue oxygenation in vessels derived from confocal microscopy of an R3230AC mammary carcinoma in a 500 × 500 × 200 × μm space [57]. This study found that decreases in the P_{50} may lead to increased hypoxia in the tissue. Though this model did vary Hb O_2 affinity, it did not explore the role of a variable heterogeneous tumor structure on the resulting O_2 delivery. Additionally, this model only changed the P_{50} of the native Hb and did not consider the potentially complex dynamics

between multiple O_2 carrying species. To account for some of these effects, this model was translated to a complex network model with the addition of a low affinity diaspirin cross linked Hb (DCLB, P_{50} = 32 mm Hg, cooperativity coefficient (n = 2.4) and a genetically crosslinked recombinant Hb (rHb) 3261BR (P_{50} = 14.6 mm Hg, n = 2.15) [58]. These studies again predicted that decreasing Hb O_2 affinity would lead to a significant increase in tissue pO_2. In this study, Tsoukias *et al.* proposed that differences in the microvascular architecture may lead to drastically different results in different tissue types during infusion of either low- or high-affinity O_2 carriers. Unfortunately, one of the weaknesses of these models is that they only consider a single tissue type for each vascular network (i.e. tumor or host tissue).

Limitations of the simulations

Despite the quantity of applicable information gathered in these models, there are still some limitations resulting from the assumptions made during model construction documented in the S1 Appendix. For example, the continuum model for tumor expansion does not accurately model highly aggressive tumors that are typically associated with increased rates of metastasis. To handle this behavior, we would likely need to consider an agent based model. It may also be difficult to achieve stable intermediate constructs in the growth of a rapidly expanding tumor construct. To stabilize this system for analysis, we would need a significantly larger simulation domain to reduce edge effects. Despite development in the parallel application of this code, there is still a considerable computational cost associated with performing these simulations. For example, doubling the edge length results in an approximately 4× increase in the computational time and an 8× increase in the memory requirement. Therefore, to reach the 100 mm^3 scale, the artificial tumor constructs would consume around 60× more resources per simulation.

Intratumoral acidosis is another factor which may have an impact on the results of the tumor simulations. Acidic pH in the tumor microenvironment and at the tumor-host boundary can result in tumor expansion and metastasis if the tumor cells are adapted to acidic conditions [59]. This acidic environment in tumors is primarily the result of increases in cellular respiration which results in increased production of carbon dioxide (CO_2) and lactate [60]. Increased CO_2 levels can result in significant reductions in Hb O_2 affinity. This can lead to substantial increases in O_2 delivery from Hb in RBCs due to the Bohr Effect [61]. Within tumors, increases in glycolysis boosts conversion of glucose to lactate. Lactate is directly related to the Warburg effect and is associated with a number of effects linked to inflammation, metastasis, and VEGF induction [62]. Lactate may also have an effect on radiotherapy and chemotherapy due to its antioxidant properties [63]. By modulating the MRO_2 with administration of PolyHb, the pH and associated concentrations of CO_2 and lactate may be altered within the tumor microenvironement. Because of these shifts, future models of tumor oxygenation should consider implementing systems of CO_2 and lactate production as additional components within the simulation.

The architecture of this model may be limited by locking the vessel bifurcations in the model to a face-centered cubic grid. This grid significantly restricts the resulting angles of the vascular architecture, which may not adequately represent the correlations between daughter vessel size ratios and bifurcations that has been reported in the literature [64]. Despite the tendency of tumors to form leaky vasculature [65, 66], we did not model extravascular transport of the PolyhHb in this model. Currently, we have not observed any PolyhHb extravasation into the tumor tissue in experimental animal models. Because of this, we chose not to model extravascular transport of the PolyhHb solutions. If PolyhHb extravasation is observed in tumor tissues, these models should be repeated with the addition of extravascular PolyhHb

transport in the tissue space. Additionally, we assumed that diffusive O_2 transport is the dominant force. In some tumors, interstitial fluid flow may result in stronger extravascular O_2 transport.

Due to limitations in the available computational resources, we were only able to numerically evaluate the effect of the PolyhHb infusions on a single type of cell line (FME human melanoma). Fortunately, the tumor architecture and bulk properties are similar to values measured in previous experimental studies. In the future, we could use anatomical data to explore our O_2 transport models within an experimentally comparable vascular network.

Finally, our assumptions for the changes between human and mouse models only focused on changes in the microvascular density, blood flow, blood O_2 offloading, and rate of O_2 consumption in normal tissue. However, there may be other physiologic properties that change between the mouse and human models including inter-cellular interactions, varied production of vascular growth factors in mouse tissue, and differences in cellular composition in the host tissue.

Conclusions

In this study, we performed simulations of PolyhHb mediated O_2 transport within human and mouse artificial tumor vascular networks. These results were validated with data from experiments performed for this study and in the literature. We can use the models developed for this study to simulate the transport of O_2 with both high and low-affinity HBOCs. The results from this mode of analysis can help highlight relationships between the vascular architecture and the ability of HBOCs like T-State and R-State PolyhHb to modulate tumor oxygenation. This makes the PolyhHb enhanced O_2 transport model developed for this study a potential tool to evaluate and estimate clinically relevant benchmarks related to the translation of PolyhHb for use as a co-therapeutic in preclinical and clinical studies. Despite changes in the organism and group separation with PCA, the primary trends and variable correlations are relatively unchanged. This may indicate that biophysical parameters as measured in a mouse may still be useful to predict trends when translated into clinical studies. Motivated by our PCA and parameter analysis, we sought to observe how the correlated variables can be used to deduce which clinically measurable values might translate into treatment benchmarks. Performing simulations on artificial constructs provide the unique opportunity to explore how different treatment options would affect the O_2 distribution and delivery given the same initial conditions. For example, our model suggests that tumors with decreased *RBF* and *RBV* are more susceptible to treatment with T-State and R-State PolyhHbs. However, we also found that large volume exchange infusion models are required to modulate hypoxia and MRO_2 at a clinically relevant level.

Furthermore, we can use this model to help predict which clinically available non-invasive measurements should be taken to guide the development of PolyhHb for use in cancer treatment. Knowing the available techniques, we can then recommend targets and ranges to better test the efficacy and performance profiles of O_2 carrying species as potential chemo-sensitizes. In our analysis of changes in the various bulk tumor properties, we determined that MRO_2 was an exciting target for assessing the effect of HBOCs on tumor oxygenation and growth. In general, tumors that were more susceptible to hypoxia reduction likely had an increase in MRO_2 after all treatment options. An increase in MRO_2 may lead to increased effectiveness of chemotherapeutics that target rapidly dividing cells. Alternatively, reducing MRO_2 and thus cell proliferation may be beneficial to limit tumor growth and thus, promote better drug delivery to tumors [52]. However, tumors that experienced a decrease in MRO_2 typically had less reduction in the hypoxic volume. Because of this difference, future animal studies on the effect of

PolyhHb enhanced oxygenation of tumors should consider the potential increase or decrease in MRO_2 when selecting tumor types and model animals. Tumor locations should also be carefully considered to model these effects. From the results of this computational analysis, we recommend implanting the same tumor cell line in two locations: (1) a tissue region with high Hb concentration ($C_{Hb,tis}$ = 50 μM) such as murine rear flank and (2) a tissue region with low Hb concentration ($C_{Hb,tis} < 45$ μM) such as murine mammary fat pad. During these studies, the transient changes in the concentrations of Hb and oxyHb in the host and tumor tissue should be measured throughout treatment using non invasive optical methods [67]. If possible, non-invasive methods for measuring MRO_2 such as positron emission tomography (PET) [68, 69], magnetic resonance imaging (MRI) [70], or near infrared fluorescent dye [71] should also be considered.

Methods

The simulations for this study were generated with a modified version of the Tumorcode simulation framework (https://github.com/thierry3000/tumorcode) [39]. The majority of simulations for this model were performed on the Owens Cluster at the Ohio Super Computing Center [72]. To simplify analysis of the resulting infusion models in artificial tumor constructs, various parameters relating oxygenation status and microvascular architecture were determined by iterating through completed files in Python v 3.6. Additional statistical comparisons such as t-tests and principal component analysis were performed with R v 3.6.0. Additional information on model construction and parameters can be found in the S1 Appendix.

Polymerized hemoglobin enhanced vascular oxygen transport model

In this work, we expand upon the work of Welter *et. al*'s previously developed model of Hb facilitated O_2 transport within the tumor microvascular architecture [39, 43]. With the addition of an HBOC, total blood O_2 concentration ($C_{O_2,total}$) can be expressed as the sum of total O_2 concentration dissolved in plasma ($C_{O_2,plasma}$), total O_2 concentration bound to Hb in RBCs ($C_{O_2,RBC}$), and total O_2 concentration bound to HBOC in the plasma ($C_{O_2,HBOC}$) as shown in Eq 1.

$$C_{O_2,total} = C_{O_2,plasma} + C_{O_2,RBC} + C_{O_2,HBOC} \tag{1}$$

The $C_{O_2,plasma}$ is proportional to pO_2 depending on the solubility of O_2 in plasma (α_{plasma}). For O_2 bound to Hb in RBCs we instead calculate $C_{O_2,\,RBC}$ by accounting for the concentration of Hb in RBCs ($C_{Hb,RBC}$) on a heme basis. To calculate O_2 bound to Hb in RBCs and HBOCs, we assumed that rate of O_2 offloading (k_{off,O_2}) is significantly faster than the residence time of Hb in RBCs and HBOCs within the vessels (Assumption 1). This would imply that hHb in RBCs and HBOCs are in equilibrium with the dissolved O_2 (equilibrium saturation (Y) = current saturation (S). We can then calculate bound O_2 by multiplying by hematocrit (HCT) and equilibrium saturation of O_2 bound to Hb in RBCs as a function of the pO_2 ($Y_{Hb}(pO_2)$) estimated with the Hill equation (Eq 2).

$$Y = \frac{pO_2^n}{pO_2^n - P_{50}^n} \tag{2}$$

The $C_{O_2,HBOC}$ can be calculated in a similar manner using the concentration of HBOC in the plasma (C_{HBOC}) and equilibrium saturation of O_2 bound to the HBOC in the plasma as a function of the pO_2 ($Y_{HBOC}(pO_2)$). Performing these substitutions, we can then calculate

$C_{O_2,total}$ as shown in Eq 3.

$$C_{O_2,total}(pO_2) = \alpha_{pls}pO_2 + HCT \cdot C_{Hb,RBC}Y_{Hb,RBC}(pO_2) + \\ + C_{HBOC}Y_{HBOC}(pO_2) \tag{3}$$

Continuing with the previously developed model, we approximate the intravascular pO_2 as varying along the length (z) of the longitudinal axis of a cylindrical vascular tube segment with total length l. Therefore, we define the intravascular O_2 flux ($j_{O_2,iv}$) as a product of the volumetric flow rate (Q) and $C_{O_2,total}$ as shown in Eq 4.

$$j_{O_2,iv} = QC_{O_2,total}(pO_2) \tag{4}$$

As blood flows through the vessel, a fraction of O_2 is delivered from plasma, Hb in RBCs, and HBOC to surrounding tissue through the vessel wall. This value is quantified as the transavascular O_2 flux ($j_{O_2,iv}$). This results in a change in the longitudinal O_2 flux which is shown in Eq 5.

$$\frac{dj_{O_2,iv}}{dz} = Q\left(\alpha_{pls}\frac{dpO_2}{dz} + HCT \cdot C_{Hb,RBC}\frac{dY_{Hb,RBC}(pO_2)}{dP}\frac{dpO_2}{dz} \right. \\ \left. + C_{HBOC}\frac{dY_{HBOC}(pO_2)}{dP}\frac{dpO_2}{dz}\right) = -2\pi r j_{O_2,tv}(z) \tag{5}$$

These equations can then be rearranged to solve for the derivative of pO_2 along the longitudinal axis as shown in Eq 6.

$$\frac{dP}{dz} = \frac{-2\pi r j_{O_2,tv}(z)}{Q\left(\alpha_{pls} + HCT \cdot C_{Hb,RBC}\frac{dY_{Hb,RBC}(pO_2)}{dP} + C_{HBOC}\frac{dY_{HBOC}(pO_2)}{dP}\right)} \tag{6}$$

Similar to the previously developed 3D model, we are assuming that diffusive transport is dominant. This is also partially accounted for within the O_2 transport Sherwood number Sh_{O_2} correlation generated within the modified KTC model described in the S5 Appendix. To simplify $j_{O_2,iv}$ we use the mass transfer coefficient (γ) to relate $j_{O_2,iv}$ as the difference between pO_2 in the blood ($pO_2(z)$ and pO_2 in the tissue ($pO_{2,tissue}$). Because vessels in the model are approximated as line sources, $pO_{2,tissue}$ is approximated as being constant along the entire vessel segment. We can then calculate γ with the previously developed Sh_{O_2}, as shown in Eq 7.

$$j_{o2_tv} = \frac{Sh_{O_2}D_{plasma}\alpha_{pls}(pO_2(z) - pO_{2,tissue})}{2r} \tag{7}$$

To calculate the vascular pO_2 distribution we first isolate the mass balance of O_2 around a single node with a set of adjacent upstream ($\mathbb{I}$) and downstream ($\mathbb{O}$) vessels. To simplify axial offloading, we assume that Hb in RBCs and HBOCs are in equilibrium with the common pO_2 $p\tilde{O}_2$ at all outlets such that $pO_{2,j} = p\tilde{O}_2$ for $j \in \mathbb{O}$ (Eq 8).

$$j_{O_2,n} = \sum_{i\in\mathbb{I}} Q_i(\alpha_{pls}pO_{2,i} + HCT_iC_{Hb,RBC}Y_{Hb,RBC}(pO_{2,i}) + C_{HBOC,i}Y_{HBOC}(pO_{2,i})) \\ = \sum_{j\in\mathbb{O}} Q_j(\alpha_{pls}p\tilde{O}_2 + HCT_jC_{Hb,RBC}Y_{Hb,RBC}(p\tilde{O}_2) + C_{HBOC,j}Y_{HBOC}(p\tilde{O}_2) \tag{8}$$

Table 1. Parameters used to compute PolyhHb enhanced oxygenation.

Symbol	Simulation Parameter	Value	Units	Source
α_{plasma}	Solubility of O_2 in plasma	1.71×10^{-3}	mol/(m^3 · mm Hg)	[57]
α_{tissue}	Solubility of O_2 in tissue	1.54×10^{-3}	mol/(m^3 · mm Hg)	[57]
n_{mHb}	Cooperativity of murine Hb in murine RBCs	2.2	-	(a)
$P_{50,mHb}$	P_{50} of murine Hb in murine RBCs	42.1	mm Hg	(a)
n_{hHb}	Cooperativity of human Hb in human RBCs	2.9	-	[73]
$P_{50,hHb}$	P_{50} of human Hb in humanRBCs	29.3	mm Hg	[73]
$D_{O_2,p}$	Diffusivity of O_2 in plasma	1.85×10^{-5}	cm^2/s	[74]
$D_{O_2,t}$	Diffusivity of O_2 in tissue space	6.30×10^{-6}	cm^2/s	[74]
$K_{M,host}$	Michaelis constant for host tissue (mouse, human)	5	mm Hg	[57]
$K_{M,tumor}$	Michaelis constant for tumor tissue	2	mm Hg	[57]
$V_{M,mouse}$	Maximum rate of O_2 consumption for mouse tissue	45	μM/s	[55]
$V_{M,human}$	Maximum rate of O_2 consumption for human tissue	15	μM/s	[55]
$V_{M,tumor}$	Maximum rate of O_2 consumption for tumor tissue	80	μM/s	[55]
HCT	Initial hematocrit	45	%	(a)
$pO_{2,BC,0}$	Minimum inlet pO_2 at the boundary	50	mm Hg	[75]
$\Delta pO_{2,BC}$	Rate of change of pO_2 at the boundary	1	mm Hg / μm	[75]
$pO_{2,BC,max}$	Maximum inlet pO_2 at the boundary	100	mm Hg	[75]

(a) Values determined with data from animal study performed in this study.

https://doi.org/10.1371/journal.pcbi.1008157.t001

The O_2 for the upstream vessels is known. Thus, rearranging the left side of Eq 8 we can obtain Eq 9.

$$j_{O_2,n} = \left[\sum_{j\in\mathbb{O}} Q_j\right]\alpha_{pls}p\tilde{O}_2 + \left[\sum_{j\in\mathbb{O}} Q_j HCT_j\right]C_{Hb,RBC}Y_{Hb,RBC}(p\tilde{O}_2) + \left[\sum_{j\in\mathbb{O}} Q_j C_{HBOC,j}\right]Y_{HBOC}(p\tilde{O}_2) \quad (9)$$

Here values in brackets correspond to the known blood, RBC, and HBOC flow rates determined from microvascular flow computation. The resulting Eq 9 can easily be solved with bisection methods.

To determine boundary conditions (BCs) for the mouse model, we began first with the simple blood vessel radius (r_{ves}) dependent linear model developed by Welter *et al.* using the minimum inlet pO_2 at the boundary ($pO_{2,BC,0}$), maximum inlet pO_2 at the boundary ($pO_{2,BC,max}$), and rate of change of pO_2 at the boundary ($\Delta pO_{2,BC}$ shown in Eq 10 [43].

$$pO_{2,BC} = \min(pO_{2,BC,0} + \Delta pO_{2,BC}r_{ves}, pO_{2,BC,max}) \quad (10)$$

Determining the pO_2 distribution in the network can then be performed with a depth-first search, as described by Welter *et al.* [43]. The parameters used to populate the O_2 transport model can be found in Table 1.

Tissue oxygen consumption

For this system, the O_2 concentration in the tissue ($C_{O_2,tissue}$) can be calculated by solving the steady-state diffusion equation on the tissue domain with Neumann boundary conditions with

O_2 exchange with vessels (V_{O_2}) and the rate of O_2 consumption (R_{O_2}) as shown in Eq 11.

$$\alpha_{tissue} D_{O_2,tissue} \nabla^2 pO_{2,tissue} - R_{O_2}(pO_{2,tissue}) + V_{O_2} = 0 \tag{11}$$

Here R_{O_2} is defined with the Michaelis-Menten model as defined in Eq 12.

$$R_{O_2} = -\frac{V_m pO_2}{K_M + pO_2} \tag{12}$$

Due to increased metabolism in mouse tissue compared to human tissue [76, 77], we assumed that the V_M of mouse tissue was approximately 3 times greater than the V_M for human tissue. We also assumed that the Michaelis-Menten coefficient (K_M) remained unchanged between mice and humans.

V_{O_2} can be expressed as line sources with integration along the axis with respect to the Dirac (δ) distribution. These vessel segments are embedded within the tissue and can be expressed as shown in Eq 13 [56].

$$V_{O_2} = \sum_{v \in \mathbb{V}} \int_v 2\pi r_{ves} j_{O_2,tv} \delta(z - y) dz \tag{13}$$

Variations in simulation construction

For our infusion simulations, we considered two dose volumes (top-load, exchange) and three material types: a non O_2 carrying control, a 35:1 T-State PolyhHb, and a 30:1 R-State PolyhHb. We also simulated a baseline condition where no treatment was delivered. Each of these 7 types of infusion simulations was performed on each simulated tumor construct modeled with the hypoxic (FME) tumor parameters. The biophysical properties of 35:1 T-State and 30:1 R-State PolyhHb were taken from the analysis performed on the PolyhHb prepared for use in the animal studies.

Unfortunately, T-State and R-State PolyhHb both have lower P_{50}s compared to native mouse Hb in RBCs. Because of this, T-State PolyhHb delivers 45% less O_2 and R-State PolyhHb delivers 96% less O_2 than the native mouse RBCs in upstream arteries and arterioles at an equivalent concentration on a per-heme basis. Furthermore, the infusion mediated hemodilution results in a 10 to 22% decrease in O_2 carried by blood. This reduction in O_2 delivery indicates that the resulting pO_2, at the BC ($pO_{2,BC}$) is likely lower than the baseline (unsupplemented) condition. To calculate these adjusted values, we must assume that the maximum $pO_{2,BC}$ is 100 mm Hg (assumption 8), and the tissue O_2 consumption outside of the modeled tumor/host microvascular system is unchanged by hemodilution or HBOC infusion (assumption 9). Thus O_2 extracted from blood between the lungs and the simulated system can be calculated by taking the O_2 extracted as shown in Eq 14.

$$OE = C_{O_2,arteries}(pO_{2,BC,max} - C_{O_2,BC}(pO_{2,BC}(r_{ves})) \tag{14}$$

Since we assume that O_2 extraction upstream of the tumor is constant for both baseline, hemodilution, and HBOC infusion, we can solve for new coefficients for the linear correlation using Eq 15.

$$OE_{baseline}(r_{ves}) = OE_{enhanced}(pO_2, r_{ves}) \tag{15}$$

In addition, we assume that despite its increased size, both 30:1 R-State and 35:1 T-State PolyhHb scavenge NO due to their increased exposure to the endothelial cell wall. This will

Table 2. Parameter variations for top-load and exchange infusion simulations of a non O_2 carrying control, 35:1 T-State PolyhHb, and R-State PolyhHb compared to baseline conditions.

Parameter	Baseline	*Top-Load infusion*			*Exchange infusion*		
		Control	35:1 T-State	30:1 R-State	Control	35:1 T-State	30:1 R-State
HCT	0.45	0.41	0.41	0.41	0.35	0.35	0.35
plasma viscosity (cP)	1.26	1.26	1.35	1.32	1.26	1.51	1.47
C_{HBOC} (mg/mL)	0	0	8	8	0	14	14
HBOC P_{50} (mm Hg)	-	-	34	1.3	-	34	1.3
HBOC n	-	-	1	1	-	1	1
$pO_{2,BC,0}$ (mm Hg)	50	49.6	50.8	49.6	46.7	49.0	46.7
$\Delta pO_{2,BC}$ (mm Hg·μm)	1.00	1.01	0.99	1.01	1.06	1.02	1.06
k_s	1	1	0.96	0.95	1	0.95	0.90

https://doi.org/10.1371/journal.pcbi.1008157.t002

lead to a decrease in the potency of the shear stress induced hemodynamic stimulus (S_H) due to a reduction in the vasorelaxation signal. In experimental models, we observed that 30:1 R-State PolyhHb had a greater tendency to lead to vasoconstriction. Therefore k_s is further reduced for this species. We approximated each of these values using the data from intravital microscopy. The varied parameters for each of the simulations can be found in Table 2

Quantifying bulk oxygenation data

As described previously, current tissue imaging techniques do not have adequate resolution to resolve the full vascular architecture of large three-dimensional tumors (> 10 mm^3). Thus, to compare our simulated results to clinically measurable parameters, we must instead observe measurable tissue averaged properties. To calculate these bulk tumor properties, we iterate through each vessel (v) in the network of vessels ($\mathbb{V}$) over the tissue volume (Ω). We use this method to calculate *MVD*, *RBV*, *RBF*, $C_{Hb,tis}$), oxyHb concentration in the tissue ($C_{oxyHb,tis}$), tissue Hb saturation ($S_{Hb,tis}$), HBOC concentration in the tissue ($C_{HBOC,tis}$), oxygenated HBOC concentration in the tissue ($C_{oxyHBOC,tis}$), and tissue Hb saturation ($S_{HBOC,tis}$). The full equations used to calculate these tissue properties can be found in S1 Appendix.

To examine functional O_2 offloading for each of the treatment cases we calculate the percentage of O_2 offloaded from each species across the full system to yield the *OEF*. For each of these systems, we calculate the mass flow of O_2 into the system ($J_{O_2,\,in}$) through each of the inlet arterioles/arteries penetrating the surface of the system ($v \in \mathbb{V} \cap \mathbb{I}$). We then subtract this value by the mass flow of O_2 out of the system ($J_{O_2,\,out}$) through the outlet venules/veins penetrating the surface of the system ($v \in \mathbb{V} \cap \mathbb{O}$) and divide by $J_{O_2,\,in}$. We also calculate O_2 extracted from each O_2 carrier (plasma, Hb in RBCs, and HBOC) to estimate how each contributes to overall O_2 delivery to the tumor. For OEF_{plas} we can calculate the mass flow of dissolved O_2 in plasma ($J_{O_2,\,plas}$) with α_{plasma}, vascular Q, and vascular pO_2 as shown in Eq 16.

$$OEF_{plas} = \frac{J_{O_2,in,pls} - J_{O_2,out,pls}}{J_{O_2,in,pls}} = \\ = \frac{\alpha_{pls}\sum_{v\in\mathbb{V}\cap\mathbb{I}} Q_v pO_{2,v} - \alpha_{pls}\sum_{v\in\mathbb{V}\cap\mathbb{O}} Q_v pO_{2,v}}{\alpha_{pls}\sum_{v\in\mathbb{V}\cap\mathbb{I}} Q_v pO_{2,v}} \tag{16}$$

We can also determine OEF_{Hb} with the mass flow of O_2 bound to Hb in RBCs ($J_{O_2,\,Hb}$) using $C_{Hb,RBC}$, vascular HCT, vascular Q, and $Y_{Hb}(pO_2)$ as shown in Eq 17.

$$\begin{aligned} OEF_{Hb} &= \frac{J_{O_2,in,Hb} - J_{O_2,out,Hb}}{J_{O_2,in,Hb}} = \\ &= \frac{C_{Hb,RBC}\sum_{v\in\mathbb{V}\cap\mathbb{I}} Q_v HCT_v Y_{Hb}(pO_{2,v}) - C_{Hb,RBC}\sum_{v\in\mathbb{V}\cap\mathbb{O}} Q_v HCT_v Y_{Hb}(pO_{2,v})}{C_{Hb,RBC}\sum_{v\in\mathbb{V}\cap\mathbb{I}} Q_v HCT_v Y_{Hb}(pO_{2,v})} \end{aligned} \tag{17}$$

The OEF_{HBOC} can be calculated with a similar method using the vascular C_{HBOC} as shown in Eq 18.

$$\begin{aligned} OEF_{HBOC} &= \frac{J_{O_2,in,HBOC} - J_{O_2,out,HBOC}}{J_{O_2,in,HBOC}} = \\ &= \frac{\sum_{v\in\mathbb{V}\cap\mathbb{I}} Q_v C_{HBOC,v} Y_{HBOC}(pO_{2,v}) - \sum_{v\in\mathbb{V}\cap\mathbb{O}} Q_v C_{HBOC,v} Y_{HBOC}(pO_{2,v})}{\sum_{v\in\mathbb{V}\cap\mathbb{I}} Q_v C_{HBOC,v} Y_{HBOC}(pO_{2,v})} \end{aligned} \tag{18}$$

We can then examine the total contribution of each O_2 carrying species to the total OEF by taking a summation of the O_2 mass flows into and out of the system as outlined in 19.

$$\begin{aligned} OEF &= \frac{J_{O_2,in} - J_{O_2,out}}{J_{O_2,in}} = \\ &= \frac{J_{O_2,in,pls} + J_{O_2,in,Hb} + J_{O_2,in,HBOC} - J_{O_2,out,pls} - J_{O_2,out,Hb} - J_{O_2,out,HBOC}}{J_{O_2,in,plas} + J_{O_2,in,Hb} + J_{O_2,in,HBOC}} \end{aligned} \tag{19}$$

In addition to O_2 delivery to the tissue, we can also examine MRO_2 by taking the volume integral of the pO_2 gradient dependent Michaelis-Menten equation (Eq 12) as shown in Eq 20.

$$MRO_2 = \frac{1}{|\Omega|}\int \Omega \frac{V_M pO_2(x)}{K_M + pO_2(x)} d^3x \tag{20}$$

Principal component analysis

Because there are a large number of variables associated with each tumor and treatment method, we employ PCA to linearly transform our data into a reduced factor space. All factors are scaled before PCA is performed. To perform this analysis, we used the prcomp function in R v. 3.6.0. The resulting data was then analyzed with PC score plots and loading factor analysis to better examine groupings and variable correlations.

Statistical analysis

Data were represented as the mean ± SEM. All box plots depict the maximum, third quantile, median, first quantile, and minimum. Data were analyzed using a one way ANOVA with a Bonferroni's correction for multiple comparisons. A p-value less than 0.05 was considered to be statistically significant between group comparisons. All statistical analysis was performed using R v. 3.6.0.

Ethics statement

To validate the simulated O_2 transport model, we compared the simulated results with fluid flow, vascular morphology, and pO_2 measured with intravital microscopy. Mice were

anesthetized with isoflurane (4% for induction, 1-2% for maintenance). All animals were euthanized with sodium pentobarbital. The protocols used to handle these mice were approved by the University of California San Diego Animal Care and Use Committee. The hHb used to prepare these materials was obtained from expired RBCs donated from Wexner Medical Center (Columbus, OH).

Supporting information

S1 Appendix. Additional description of the model. This file outlines additional segments of the model that have been applied from the Tumorcode framework including artificial blood vessel network generation, continuum model for tumor expansion, vascular remodeling during tumor growth, and quantifying bulk morphological data.
(PDF)

S2 Appendix. Additional details on tumor growth and resulting properties. This file outlines the growth and resulting properties of the artificial mouse and tumor constucts described in this study.
(PDF)

S3 Appendix. Synthesis and biophysical properties of T-State and R-State PolyhHb. This file documents the synthesis procedure and biophysical properties of the HBOCs prepared for this study.
(PDF)

S4 Appendix. Comparison of mouse and human host tissue oxygenation and blood flow. This file documents the comparison between the oxygenation and blood flow observed between the simulated human and host tissue in which the artificial tumor constructs were produced.
(PDF)

S5 Appendix. Determination of an oxygen transport Sherwood number. This file documents the method to determine the HBOC modified Sherwood number as estimated with linear regression on results from parametric sweeps on a KTC model.
(PDF)

S6 Appendix. Computational model validation with animal experiments. This file documents an intravital microscopy and tumor growth experimental study that was used to validate the HBOC modified O_2 transport model and vascularized tumor system used in this study.
(PDF)

S1 Dataset. Dataset of the results from the oxygenation simulation. This file contains a dataset of the various tumor properties calculated in the hemoglobin-based oxygen carrier tumor simulation.
(CSV)

Acknowledgments

We acknowledge Dr. Christopher Hadad (Dept. of Chemistry and Biochemistry, The Ohio State University) for kindly allowing the use of his stopped-flow spectrophotometer and Dr. Robert J. Lee (College of Pharmacy, The Ohio State University) for permitting the use of his dynamic light scattering (DLS) spectrometer. We further acknowledge Marni Grevenow (Transfusion Services, Wexner Medical Center, The Ohio State University) for generously donating expired human RBC units. We would like to thank the Ohio Supercomputing Center

(OSC), an OHTECH Consortium member, for providing the computational resources needed for the simulations. We would specifically like to thank Dr. Xia Wang and David Heisterberg for their help configuring and installing the simulation code on the Owens cluster. Additionally we would like to thank Thierry Fredrich at Saarland University for his help with navigating and applying the Tumorcode framework. We would also like to thank Cynthia Walser for the surgical perpetrations and tumor implantation.

Author Contributions

Conceptualization: Donald A. Belcher, Pedro Cabrales, Andre F. Palmer.

Data curation: Donald A. Belcher.

Formal analysis: Donald A. Belcher.

Funding acquisition: Donald A. Belcher, Andre F. Palmer.

Investigation: Donald A. Belcher, Alfredo Lucas, Pedro Cabrales.

Methodology: Donald A. Belcher, Alfredo Lucas.

Project administration: Pedro Cabrales, Andre F. Palmer.

Resources: Andre F. Palmer.

Software: Donald A. Belcher.

Supervision: Pedro Cabrales, Andre F. Palmer.

Validation: Donald A. Belcher, Alfredo Lucas.

Visualization: Donald A. Belcher.

Writing – original draft: Donald A. Belcher.

Writing – review & editing: Donald A. Belcher, Pedro Cabrales, Andre F. Palmer.

References

1. Nozue M, Lee I, Manning JM, Manning LR, Jain RK. Oxygenation in tumors by modified hemoglobins. Journal of Surgical Oncology. 1996; 62(2):109–114. https://doi.org/10.1002/(SICI)1096-9098(199606)62:2%3C109::AID-JSO6%3E3.0.CO;2-C
2. Liu XB, Cheng Q, Geng W, Ling CC, Liu Y, Ng KTP, et al. Enhancement of cisplatin-based TACE by a hemoglobin-based oxygen carrier in an orthotopic rat HCC model. Artificial Cells, Nanomedicine and Biotechnology. 2014; 42(4):229–236. https://doi.org/10.3109/21691401.2013.808647
3. Lee NP, Chan KT, Choi MY, Lam HY, Tung LN, Tzang FC, et al. Oxygen carrier YQ23 can enhance the chemotherapeutic drug responses of chemoresistant esophageal tumor xenografts. Cancer Chemotherapy and Pharmacology. 2015; 76(6):1199–1207. https://doi.org/10.1007/s00280-015-2897-2 PMID: 26553104
4. Qi X, Wong BL, Lau SH, Ng KTPP, Kwok SY, Kin-Wai Sun C, et al. A hemoglobin-based oxygen carrier sensitized Cisplatin based chemotherapy in hepatocellular carcinoma. Oncotarget. 2017; 8(49):85311–85325. https://doi.org/10.18632/oncotarget.19672 PMID: 29156721
5. Robinson MF, Dupuis NP, Kusumoto T, Liu F, Menon K, Teicher Ba. Increased Tumor Oxygenation and Radiation Sensitivity in two Rat Tumors by A Hemoglobin-Based, Oxygen-Carrying Preparation. Artificial Cells, Blood Substitutes and Biotechnology. 1995; 23(3):431–438. https://doi.org/10.3109/10731199509117959
6. Teicher BA, Holden SA, Ara G, Herman TS, Hopkins RE, Menon K. Effect of a bovine hemoglobin preparation (sbhs) on the response of two murine solid tumors to radiation therapy or chemotherapeutic alkylating agents. Biomaterials, Artificial Cells and Immobilization Biotechnology. 1992; 20(4–Feb):657–660. https://doi.org/10.3109/10731199209119697
7. Teicher BA, Herman TS, Hopkins RE, Menon K. Effect of oxygen level on the enhancement of tumor response to radiation by perfluorochemical emulsions or a bovine hemoglobin preparation. International

Journal of Radiation Oncology, Biology, Physics. 1991; 21(4):969–974. https://doi.org/10.1016/0360-3016(91)90737-O

8. Teicher BA, Holden SA, Dupuis NP, Kusomoto T, Liu M, Liu F, et al. Oxygenation of the rat 9L gliosarcoma and the rat 13672 mammary carcinoma with various doses of a hemoglobin solution. Artificial cells, blood substitutes, and immobilization biotechnology. 1994; 22(3):827–833. https://doi.org/10.3109/10731199409117917 PMID: 7994406
9. Teicher BA, Schwartz GN, Sotomayor EA, Robinson MF, Dupuis NP, Menon K. Oxygenation of tumors by a hemoglobin solution. Journal of Cancer Research and Clinical Oncology. 1993; 120(1-2):85–90. https://doi.org/10.1007/BF01200729
10. Teicher BA, Holden SA, Menon K, Hopkins RE, Gawryl MS. Effect of hemoglobin solution on the response of intracranial and subcutaneous 9L tumors to antitumor alkylating agents. Cancer Chemotherapy and Pharmacology. 1993; 33(1):57–62. https://doi.org/10.1007/BF00686024
11. Teicher BA, Holden SA, Ara G, Dupuis NP, Liu F, Yuan J, et al. Influence of an anti-angiogenic treatment on 9L gliosarcoma: oxygenation and response to cytotoxic therapy. International Journal of Cancer. 1995; 61(5):732–737. https://doi.org/10.1002/ijc.2910610523 PMID: 7768649
12. Belcher DA, Ju JA, Baek JH, Yalamanoglu A, Buehler PW, Gilkes DM, et al. The quaternary state of polymerized human hemoglobin regulates oxygenation of breast cancer solid tumors: A theoretical and experimental study. PLoS ONE. 2018; 13(2). https://doi.org/10.1371/journal.pone.0191275
13. Linberg R, Conover CD, Shum KL, Shorr RG, R L, Cd C, et al. Increased tissue oxygenation and enhanced radiation sensitivity of solid tumors in rodents following polyethylene glycol conjugated bovine hemoglobin administration. In vivo. 1997; 12(2):167–173.
14. Yu MH, Han JQ, Dai M, Cui PL, Li HW, Liu Q, et al. Influence of PEG-conjugated Hemoglobin on Tumor Oxygenation and Response to Chemotherapy. Artificial Cells Blood Substitutes and Biotechnology. 2008; 36(6):551–561. https://doi.org/10.1080/10731190802556674
15. Han J, Yu M, Dai M, Li H, Xiu R, Liu Q. Decreased expression of MDR1 in PEG-conjugated hemoglobin solution combined cisplatin treatment in a tumor xenograft model. Artificial Cells, Blood Substitutes, and Biotechnology. 2012; 40(4):239–244. https://doi.org/10.3109/10731199.2012.663385
16. Zhao Y, Chen G, Meng Z, Gong G, Zhao W, Wang K, et al. A novel nanoparticle drug delivery system based on PEGylated hemoglobin for cancer therapy. Drug Delivery. 2019; 26(1):717–723. https://doi.org/10.1080/10717544.2019.1639846 PMID: 31293178
17. Yamamoto M, Izumi Y, Horinouchi H, Teramura Y, Sakai H, Kohno M, et al. Systemic Administration of Hemoglobin Vesicle Elevates Tumor Tissue Oxygen Tension and Modifies Tumor Response to Irradiation. Journal of Surgical Research. 2009; 151(1):48–54. https://doi.org/10.1016/j.jss.2007.12.770 PMID: 18262559
18. Kawaguchi F, Kawaguchi AT, Murayama C, Kamijo A, Haida M. Liposome-Encapsulated Hemoglobin Improves Tumor Oxygenation as Detected by Near-Infrared Spectroscopy in Colon Carcinoma in Mice. Artificial Organs. 2017; 41(4):327–335. https://doi.org/10.1111/aor.12825
19. Yang J, Li W, Luo L, Jiang M, Zhu C, Qin B, et al. Hypoxic tumor therapy by hemoglobin-mediated drug delivery and reversal of hypoxia-induced chemoresistance. Biomaterials. 2018; 182:145–156. https://doi.org/10.1016/j.biomaterials.2018.08.004 PMID: 30121013
20. Jiang MS, Yin XY, Qin B, Xuan SY, Yuan XL, Yin H, et al. Inhibiting Hypoxia and Chemotherapy-Induced Cancer Cell Metastasis under a Valid Therapeutic Effect by an Assistance of Biomimetic Oxygen Delivery. Molecular Pharmaceutics. 2019; 16(11):4530–4541. https://doi.org/10.1021/acs.molpharmaceut.9b00663 PMID: 31617723
21. Raabe A, Gottschalk A, Hommel M, Dubben HHH, Strandl T, Raabe* A, et al. No effect of the hemoglobin solution HBOC-201 on the response of the rat R1H tumor to fractionated irradiation. Strahlentherapie und Onkologie. 2005; 181(11):730–737. https://doi.org/10.1007/s00066-005-1418-3 PMID: 16254709
22. Alayash AI. Blood substitutes: Why haven't we been more successful?; 2014. Available from: http://www.ncbi.nlm.nih.gov/pubmed/24630491 http://www.pubmedcentral.nih.gov/articlerender.fcgi?artid=PMC4418436.
23. Palmer AF, Intaglietta M, Greenburg AG, Kim HW, Palmer AF, Intaglietta M. Blood Substitutes. Annual Review of Biomedical Engineering. 2014; 16(1):77–101. https://doi.org/10.1146/annurev-bioeng-071813-104950
24. Baek JH, Zhou Y, Harris DR, Schaer DJ, Palmer AF, Buehler PW. Down selection of polymerized bovine hemoglobins for use as oxygen releasing therapeutics in a Guinea pig model. Toxicological Sciences. 2012; 127(2):567–581. https://doi.org/10.1093/toxsci/kfs109
25. Belcher DA, Cuddington CT, Martindale EL, Pires IS, Palmer AF. Controlled Polymerization and Ultrafiltration Increase the Consistency of Polymerized Hemoglobin for Use as an Oxygen Carrier. Bioconjugate Chemistry. 2020; p. acs.bioconjchem.9b00766. https://doi.org/10.1021/acs.bioconjchem.9b00766

26. Fleming IN, Manavaki R, Blower PJ, West C, Williams KJ, Harris AL, et al. Imaging tumour hypoxia with positron emission tomography. British Journal of Cancer. 2015; 112(2):238–250. https://doi.org/10.1038/bjc.2014.610 PMID: 25514380

27. Christen T, Bolar DS, Zaharchuk G. Imaging Brain Oxygenation with MRI Using Blood Oxygenation Approaches: Methods, Validation, and Clinical Applications. American Journal of Neuroradiology. 2013; 34(6):1113–1123. https://doi.org/10.3174/ajnr.A3070

28. Grosenick D, Wabnitz H, Moesta KT, Mucke J, Schlag PM, Rinneberg H. Time-domain scanning optical mammography: II. Optical properties and tissue parameters of 87 carcinomas. Physics in Medicine and Biology. 2005; 50(11):2451–2468. https://doi.org/10.1088/0031-9155/50/11/002

29. Spinelli L, Torricelli A, Pifferi A, Taroni P, Danesini G, Cubeddu R. Characterization of female breast lesions from multi-wavelength time-resolved optical mammography. Physics in Medicine and Biology. 2005; 50(11):2489–2502. https://doi.org/10.1088/0031-9155/50/11/004

30. Namdee K, Carrasco-Teja M, Fish MB, Charoenphol P, Eniola-Adefeso O. Effect of Variation in Hemorheology Between Human and Animal Blood on the Binding Efficacy of Vascular-Targeted Carriers. Scientific Reports. 2015; 5(1):11631. https://doi.org/10.1038/srep11631

31. Gonzalez NC, Kuwahira I. Systemic Oxygen Transport with Rest, Exercise, and Hypoxia: A Comparison of Humans, Rats, and Mice. In: Comprehensive Physiology. vol. 8. Hoboken, NJ, USA: John Wiley & Sons, Inc.; 2018. p. 1537–1573. Available from: http://doi.wiley.com/10.1002/cphy.c170051.

32. White CR, Seymour RS. Allometric scaling of mammalian metabolism. Journal of Experimental Biology. 2005; 208(9):1611–1619. https://doi.org/10.1242/jeb.01501

33. Suarez RK, Darveau CA. Multi-level regulation and metabolic scaling. Journal of Experimental Biology. 2005; 208(9):1627–1634. https://doi.org/10.1242/jeb.01503

34. Shirasawa T, Izumizaki M, Suzuki Yi, Ishihara A, Shimizu T, Tamaki M, et al. Oxygen affinity of hemoglobin regulates O2 consumption, metabolism, and physical activity. The Journal of biological chemistry. 2003; 278(7):5035–43. https://doi.org/10.1074/jbc.M211110200 PMID: 12458204

35. Perfahl H, Byrne HM, Chen T, Estrella V, Alarcón T, Lapin A, et al. Multiscale modelling of vascular tumour growth in 3D: The roles of domain size and boundary conditions. PLoS ONE. 2011; 6(4):e14790. https://doi.org/10.1371/journal.pone.0014790 PMID: 21533234

36. Jiang Y, Pjesivac-Grbovic J, Cantrell C, Freyer JP. A multiscale model for avascular tumor growth. Biophysical journal. 2005; 89(6):3884–3894. https://doi.org/10.1529/biophysj.105.060640

37. Owen MR, Alarcón T, Maini PK, Byrne HM. Angiogenesis and vascular remodelling in normal and cancerous tissues. Journal of Mathematical Biology. 2009; 58(4-5):689–721. https://doi.org/10.1007/s00285-008-0213-z

38. Alarcon T, Byrne HM, Maini PK. A multiple scale model for tumor growth. Society of Industrial and Applied Mathematics. 2005; 3(2):440–475.

39. Fredrich T, Welter M, Rieger H. Tumorcode: A framework to simulate vascularized tumors. European Physical Journal E. 2018; 41(4):216903. https://doi.org/10.1140/epje/i2018-11659-x

40. Jain RK. Determinants of Tumor Blood Flow: A Review. Cancer Research. 1988; 48(10):2641–2658.

41. Deipolyi AR, Zhu AX, Oklu R. Intratumoral Vascular Shunting: Biomarker of Clinical Outcome and Source of Circulating Tumor Cells? American Journal of Clinical Oncology. 2015; 38(6):621–626. https://doi.org/10.1097/COC.0000000000000145

42. Welter M, Rieger H. Interstitial Fluid Flow and Drug Delivery in Vascularized Tumors: A Computational Model. PLoS ONE. 2013; 8(8):e70395. https://doi.org/10.1371/journal.pone.0070395

43. Welter M, Fredrich T, Rinneberg H, Rieger H, Hoff DV, Hingorani S. Computational Model for Tumor Oxygenation Applied to Clinical Data on Breast Tumor Hemoglobin Concentrations Suggests Vascular Dilatation and Compression. PLOS ONE. 2016; 11(8):e0161267. https://doi.org/10.1371/journal.pone.0161267

44. Greijer AE, van der Wall E. The role of hypoxia inducible factor 1 (HIF-1) in hypoxia induced apoptosis. Journal of clinical pathology. 2004; 57(10):1009–14. https://doi.org/10.1136/jcp.2003.015032

45. Worschech A, Chen N, Yu YA, Zhang Q, Pos Z, Weibel S, et al. Systemic treatment of xenografts with vaccinia virus GLV-1h68 reveals the immunologic facet of oncolytic therapy. BMC genomics. 2009; 10:301. https://doi.org/10.1186/1471-2164-10-301 PMID: 19583830

46. Murphy H, Jaafari H, Dobrovolny HM. Differences in predictions of ODE models of tumor growth: a cautionary example. BMC Cancer. 2016; 16(1):163. https://doi.org/10.1186/s12885-016-2164-x

47. Missbach-Guentner J, Dullin C, Kimmina S, Zientkowska M, Domeyer-Missbach M, Malz C, et al. Morphologic changes of mammary carcinomas in mice over time as monitored by flat-panel detector volume computed tomography. Neoplasia. 2008; 10(7):663–673. https://doi.org/10.1593/neo.08270 PMID: 18592006

48. Egeblad M, Nakasone ES, Werb Z. Tumors as organs: Complex tissues that interface with the entire organism. Developmental Cell. 2010; 18(6):884–901. https://doi.org/10.1016/j.devcel.2010.05.012

49. Stylianopoulos T, Jain RK. Combining two strategies to improve perfusion and drug delivery in solid tumors. Proceedings of the National Academy of Sciences of the United States of America. 2013; 110 (46):18632–18637. https://doi.org/10.1073/pnas.1318415110

50. Soliz J, Thomsen JJ, Soulage C, Lundby C, Gassmann M. Sex-dependent regulation of hypoxic ventilation in mice and humans is mediated by erythropoietin. American Journal of Physiology-Regulatory, Integrative and Comparative Physiology. 2009; 296(6):R1837–R1846. https://doi.org/10.1152/ajpregu.90967.2008

51. Frappell P, Lanthier C, Baudinette RV, Mortola JP. Metabolism and ventilation in acute hypoxia: a comparative analysis in small mammalian species. American Journal of Physiology-Regulatory, Integrative and Comparative Physiology. 1992; 262(6):R1040–R1046. https://doi.org/10.1152/ajpregu.1992.262.6.R1040

52. Chen Y, Cairns R, Papandreou I, Koong A, Denko NC. Oxygen consumption can regulate the growth of tumors, a new perspective on the Warburg effect. PloS one. 2009; 4(9):e7033. https://doi.org/10.1371/journal.pone.0007033

53. Goldman D. Theoretical models of microvascular oxygen transport to tissue. Microcirculation. 2008; 15 (8):795–811. https://doi.org/10.1080/10739680801938289

54. Hsu R, Secomb TW. A Green's function method for analysis of oxygen delivery to tissue by microvascular networks. Mathematical biosciences. 1989; 96(1):61–78. https://doi.org/10.1016/0025-5564(89)90083-7

55. Secomb TW, Hsu R, Dewhirst MW, Klitzman B, Gross JF. Analysis of oxygen transport to tumor tissue by microvascular networks. International Journal of Radiation Oncology, Biology, Physics. 1993; 25 (3):481–489. https://doi.org/10.1016/0360-3016(93)90070-C

56. Secomb TW, Hsu R, Park EYH, Dewhirst MW. Green's function methods for analysis of oxygen delivery to tissue by microvascular networks. Annals of Biomedical Engineering. 2004; 32(11):1519–1529. https://doi.org/10.1114/B:ABME.0000049036.08817.44

57. Kavanagh BD, Secomb TW, Hsu R, Lin PSS, Venitz J, Dewhirst MW. A theoretical model for the effects of reduced hemoglobin-oxygen affinity on tumor oxygenation. International Journal of Radiation Oncology, Biology, Physics. 2002; 53(1):172–179. https://doi.org/10.1016/S0360-3016(02)02740-2

58. Tsoukias NM, Goldman D, Vadapalli A, Pittman RN, Popel AS. A computational model of oxygen delivery by hemoglobin-based oxygen carriers in three-dimensional microvascular networks. Journal of Theoretical Biology. 2007; 248(4):657–674. https://doi.org/10.1016/j.jtbi.2007.06.012

59. Rofstad EK, Mathiesen B, Kindem K, Galappathi K. Acidic extracellular pH promotes experimental metastasis of human melanoma cells in athymic nude mice. Cancer Research. 2006; 66(13):6699–6707. https://doi.org/10.1158/0008-5472.CAN-06-0983

60. Helmlinger G, Sckell A, Dellian M, Forbes NS, Jain RK. Acid production in glycolysis-impaired tumors provides new insights into tumor metabolism. Clinical Cancer Research. 2002; 8(4):1284–1291.

61. Jensen FB. Red blood cell pH, the Bohr effect, and other oxygenation-linked phenomena in blood O2 and CO2 transport; 2004. Available from: http://doi.wiley.com/10.1111/j.1365-201X.2004.01361.x.

62. Kato Y, Ozawa S, Miyamoto C, Maehata Y, Suzuki A, Maeda T, et al. Acidic extracellular microenvironment and cancer. Cancer Cell International. 2013; 13(1):89. https://doi.org/10.1186/1475-2867-13-89 PMID: 24004445

63. Sattler UGA, Meyer SS, Quennet V, Hoerner C, Knoerzer H, Fabian C, et al. Glycolytic metabolism and tumour response to fractionated irradiation. Radiotherapy and Oncology. 2010; 94(1):102–109. https://doi.org/10.1016/j.radonc.2009.11.007 PMID: 20036432

64. Huo Y, Finet G, Lefevre T, Louvard Y, Moussa I, Kassab GS. Which diameter and angle rule provides optimal flow patterns in a coronary bifurcation? Journal of biomechanics. 2012; 45(7):1273–9. https://doi.org/10.1016/j.jbiomech.2012.01.033

65. Azzi S, Hebda JK, Gavard J. Vascular permeability and drug delivery in cancers. Frontiers in oncology. 2013; 3:211. https://doi.org/10.3389/fonc.2013.00211

66. Fukumura D, Yuan F, Endo M, Jain RK. Role of nitric oxide in tumor microcirculation. Blood flow, vascular permeability, and leukocyte-endothelial interactions. The American journal of pathology. 1997; 150 (2):713–725.

67. Taroni P, Quarto G, Pifferi A, Abbate F, Balestreri N, Menna S, et al. Breast Tissue Composition and Its Dependence on Demographic Risk Factors for Breast Cancer: Non-Invasive Assessment by Time Domain Diffuse Optical Spectroscopy. PLOS ONE. 2015; 10(6):e0128941. https://doi.org/10.1371/journal.pone.0128941 PMID: 26029912

68. Kim MM, Parolia A, Dunphy MP, Venneti S. Non-invasive metabolic imaging of brain tumours in the era of precision medicine. Nature reviews Clinical oncology. 2016; 13(12):725–739. https://doi.org/10.1038/nrclinonc.2016.108

69. Lv PC, Putt KS, Low PS. Evaluation of Nonpeptidic Ligand Conjugates for SPECT Imaging of Hypoxic and Carbonic Anhydrase IX-Expressing Cancers. Bioconjugate Chemistry. 2016; 27(7):1762–1769. https://doi.org/10.1021/acs.bioconjchem.6b00271

70. Ramamonjisoa N, Ackerstaff E. Characterization of the Tumor Microenvironment and Tumor–Stroma Interaction by Non-invasive Preclinical Imaging. Frontiers in Oncology. 2017; 7:3. https://doi.org/10.3389/fonc.2017.00003

71. Lv PC, Roy J, Putt KS, Low PS. Evaluation of a Carbonic Anhydrase IX-Targeted Near-Infrared Dye for Fluorescence-Guided Surgery of Hypoxic Tumors. Molecular Pharmaceutics. 2016; 13(5):1618–1625. https://doi.org/10.1021/acs.molpharmaceut.6b00065

72. Ohio Supercomputer Center; 1987. Available from: http://osc.edu/ark:/19495/f5s1ph73.

73. Patton JN, Palmer AF. Numerical simulation of oxygen delivery to muscle tissue in the presence of hemoglobin-based oxygen carriers. Biotechnology Progress. 2006; 22(4):1025–1049. https://doi.org/10.1021/bp060022a

74. Vadapalli A, Goldman D, Popel AS. Calculations of Oxygen Transport By Red Blood Cells and Hemoglobin Solutions in Capillaries. Artificial Cells, Blood Substitutes, and Biotechnology. 2002; 30(3):157–188. https://doi.org/10.1081/BIO-120004338

75. Yaseen MA, Srinivasan VJ, Sakadžić S, Radhakrishnan H, Gorczynska I, Wu W, et al. Microvascular Oxygen Tension and Flow Measurements in Rodent Cerebral Cortex during Baseline Conditions and Functional Activation. Journal of Cerebral Blood Flow & Metabolism. 2011; 31(4):1051–1063. https://doi.org/10.1038/jcbfm.2010.227

76. Wang Z, Zhang J, Ying Z, Heymsfield SB. Organ-Tissue Level Model of Resting Energy Expenditure Across Mammals: New Insights into Kleiber's Law. ISRN Zoology. 2012; 2012:1–9. https://doi.org/10.5402/2012/673050

77. Kummitha CM, Kalhan SC, Saidel GM, Lai N. Relating tissue/organ energy expenditure to metabolic fluxes in mouse and human: experimental data integrated with mathematical modeling. Physiological Reports. 2014; 2(9):e12159. https://doi.org/10.14814/phy2.12159